doi:10.1016/S0016-7037(00)00268-0

Vanadium in peridotites as a proxy for paleo-fO_2 during partial melting: Prospects, limitations, and implications

Cin-Ty Aeolus Lee,[1,]* Alan D. Brandon,[2] and Marc Norman[3]

[1]Department of Earth Science, MS-126, Rice University, P.O. Box 1892, Houston, TX 77251, USA
[2]NASA-JSC, 2101 NASA Road 1, Mail Code SR, Building 31, Room 114, Houston, TX 77058, USA
[3]Research School of Earth Sciences, Mills Road-Building 61, The Australian National University, Canberra, ACT 0200, Australia

Abstract—The compatibility of vanadium (V) during mantle melting is a function of oxygen fugacity (fO_2): at high fO_2's, V becomes more incompatible. The prospects and limitations of using the V content of peridotites as a proxy for paleo-fO_2 at the time of melt extraction were investigated here by assessing the uncertainties in V measurements and the sensitivity of V as a function of degree of melt extracted and fO_2. V-MgO and V-Al$_2$O$_3$ systematics were found to be sensitive to fO_2 variations, but consideration of the uncertainties in measurements and model parameters indicates that V is sensitive only to relative fO_2 differences greater than ~2 log units. Post-Archean oceanic mantle peridotites, as represented by abyssal peridotites and obducted massif peridotites, have V-MgO and -Al$_2$O$_3$ systematics that can be modeled by 1.5 GPa melting between FMQ − 3 and FMQ − 1. This is consistent with fO_2's of the mantle source for mid-ocean ridge basalts (MORBs) as determined by the Fe^{3+} activity of peridotitic minerals and basaltic glasses. Some arc-related peridotites have slightly lower V for a given degree of melting than oceanic mantle peridotites, and can be modeled by 1.5 GPa melting at fO_2's as high as FMQ. However, the majority of arc-related peridotites have V-MgO systematics overlapping that of oceanic mantle peridotites, suggesting that although some arc mantle may melt under slightly oxidizing conditions, most arc mantle does not. The fact that thermobarometrically determined fO_2's in arc peridotites and lavas can be significantly higher than that inferred from V systematics, suggests that V retains a record of the fO_2 during partial melting, whereas the activity of Fe^{3+} in arc peridotitic minerals and lavas reflect subsequent metasomatic overprints and magmatic differentiation/emplacement processes, respectively.

Peridotites associated with middle to late Archean cratonic mantle are characterized by highly variable V-MgO systematics. Tanzanian cratonic peridotites have V systematics indistinguishable from post-Archean oceanic mantle and can be modeled by 3 GPa partial melting at ~FMQ − 3. In contrast, many South African and Siberian cratonic peridotites have much lower V contents for a given degree of melting, suggesting at first glance that partial melting occurred at high fO_2's. More likely, however, their unusually low V contents for a given degree of melting may be artifacts of excess orthopyroxene, a feature that pervades many South African and Siberian peridotites but not the Tanzanian peridotites. This is indicated by the fact that the V contents of South African and Siberian peridotites are correlated with increases in SiO$_2$ content, generating data arrays that cannot be modeled by partial melting but can instead be generated by the addition of orthopyroxene through processes unrelated to primary melt depletion. Correction for orthopyroxene addition suggests that the South African and Siberian peridotites have V-MgO systematics similar to those of Tanzanian peridotites. Thus, if the Tanzanian peridotites represent the original partial melting residues, and if the South African and Siberian peridotites have been modified by orthopyroxene addition, then there is no indication that Archean cratonic mantle formed under fO_2's significantly greater than that of modern oceanic mantle. Instead, the fO_2's inferred from the V systematics in these three cratonic peridotite suites are within range of modern oceanic mantle. This also suggests that the transition from a highly reducing mantle in equilibrium with a metallic core to the present oxidized state must have occurred by late Archean times. *Copyright © 2003 Elsevier Ltd*

1. INTRODUCTION

Vanadium exists in potentially four valence states, V^{2+}, V^{3+}, V^{4+}, and V^{5+}. At terrestrial oxygen fugacities (fO_2), the dominant valence states are V^{3+}, V^{4+}, and V^{5+} in decreasing order of abundance, and with increasing fO_2, the $V^{3+}/\Sigma V$ ratio decreases (Canil, 2002). Canil and coworkers showed that the experimentally measured partition coefficients of V between crystal and liquid, $D_V^{crystal/liquid}$, decreases with increasing fO_2 because crystal structures prefer V^{3+} over the higher oxidation states of V (Canil, 1997, 1999; Canil and Fedortchouk, 2000, 2001). Because the proportion of V^{3+} decreases with increasing fO_2, V becomes more incompatible with increasing fO_2, and therefore, the V systematics of magmas or residual peridotites may potentially be used to constrain fO_2 during magma differentiation and partial melting, respectively.

The bulk V content of a peridotite may better preserve a record of the fO_2 conditions at the time of melting than Fe^{3+} activities in various mineral phases. In peridotites, V is moderately incompatible ($D^{bulk \ solid/melt} \sim 0.5$). Thus, V in a residual peridotite is likely to be more resistant to metasomatism than highly incompatible elements because V is likely not as enriched in melts to the extent that highly incompatible ele-

ments are. Furthermore, in a system open to O_2 exchange, both the bulk Fe^{3+}/Fe^{2+} ratios and the activity of Fe^{3+} in each mineral phase is controlled by the externally imposed fO_2 (for example via the passage of oxidizing metasomatic fluids). In contrast, the bulk rock V content will remain unaffected by changes in fO_2, provided the system remains closed to V. It follows that oxygen thermobarometry reflects only the last equilibration event, which may or may not coincide with the time of melt extraction, while bulk V may more closely reflect the conditions during the original partial melting event. The prospects and limitations of using V as a proxy for paleo-fO_2 are thus the focus of this paper.

Canil applied experimental calibrations of $D_V^{crystal/liquid}$ as a function of fO_2 towards modeling V depletion during partial melting of peridotites from Archean and Phanerozoic terranes (Canil, 1999, 2002), leading to two major conclusions: 1) fO_2 is roughly correlated with tectonic environment (arc-related peridotites partially melted at higher fO_2's than oceanic peridotites), and 2) peridotites that underwent melt extraction in the Archean did so at fO_2's distinctly higher than Phanerozoic oceanic peridotites. These conclusions have important implications for understanding the links between mantle processes, tectonics, and atmospheric compositional changes over Earth history. The first conclusion implies that V can be used to decipher the tectonic origin of ancient peridotites (Canil, 1999). In particular, based on Fe^{3+}/Fe^{2+} ratios in peridotitic minerals and in lavas, it is generally believed that subarc mantle is more oxidized than oceanic mantle, and therefore, the former would be expected to have lower V contents for a given degree of melting (Wood and Virgo, 1989; Carmichael, 1991; Brandon and Draper, 1996). The second conclusion has implications for the compositional evolution of the Earth's atmosphere with time because the composition of volcanic gases is controlled by mantle fO_2 (Kasting et al., 1993; Kump et al., 2001).

Interpretations of V data, however, may be complicated by a number of factors, which have not yet been considered in depth. First, interlaboratory bias limits the fO_2-resolving power of V data. Second, partitioning of V during partial melting was modeled at constant fO_2. But in a closed system (closed to O_2 exchange), it is possible that fO_2 varies during partial melting due to redistribution of Fe^{3+} among different solid and liquid phases, whose proportions also change during melting. Third, the possibility of the system being open to V exchange after the primary melting event was not considered: some peridotites have experienced melt-rock reaction and/or cumulate processes that have changed their major-element and modal compositions, resulting in changes in the bulk V content.

In this investigation, the significance of these and other complications are carefully assessed in interpreting V systematics in peridotites. As shown below, while some arc-related peridotites have low V contents consistent with melting at high fO_2, the majority of arc-related peridotites have V systematics indistinguishable from oceanic peridotites. This implies that partial melting in arcs may not be pervasively characterized by high fO_2 as is commonly believed (Parkinson and Arculus, 1999). The high fO_2's determined thermobarometrically on arc-related peridotites must have been incurred from metasomatic overprints (Brandon and Draper, 1996, 1998), and the even higher fO_2's of arc lavas must have been incurred from metasomatic overprints in their mantle source regions and/or

during emplacement and differentiation of the magma. Finally, many Archean cratonic peridotites show evidence for orthopyroxene addition through melt-rock reaction and/or cumulate processes. It is shown here that addition of orthopyroxene manifests itself as depressed trajectories in plots of V against MgO, Al_2O_3, and SiO_2, giving the artifact of low fO_2. Quantitative modeling of melt-rock reaction and cumulate processes show that these processes can easily explain the V systematics of the orthopyroxene-rich peridotites, suggesting that Archean cratonic peridotites did not melt at high fO_2's as originally suggested by Canil (2002).

2. DATA AND METHODS

2.1. Data Set

The peridotite V data used in this study are from the literature and our own data from Tanzania (Lee and Rudnick, 1999; Lee, 2001), the Simcoe volcanic field associated with the Cascades arc (Brandon and Draper, 1996), Ichinomegata (Japan arc), and southwestern USA. These data are presented in the Appendix. All literature data sources are given in the figure captions. The data were subdivided into an Archean group and a post-Archean group. The Archean group consists of peridotite xenoliths (mineralogy = orthopyroxene, clinopyroxene, olivine and garnet [or chromite]) sampled from kimberlitic or diatremes or alkaline basaltic lavas erupted through middle to late Archean cratons (Tanzania, Siberia, and South Africa). All such peridotites appear to be derived from pressures between 2.5 to 5 GPa based on garnet-orthopyroxene thermobarometry or pressures inferred from two pyroxene-thermoetry and equilibrium geotherms. They are further characterized by very unradiogenic $^{187}Os/^{188}Os$ signatures, which indicate that their Re/Os ratios were fractionated from the convecting mantle by partial melting during middle to late Archean times (Walker et al., 1989; Pearson et al., 1995a,b; Chesley et al., 1999).

The post-Archean group consists of spinel peridotites (mineralogy = orthopyroxene, clinopyroxene, olivine, spinel) derived from post-Archean terranes. Due to the lack of garnet and presence of aluminous spinel, these peridotites must be derived from pressures less than ~2.5 GPa (O'Neill, 1981). The post-Archean peridotites are subdivided into the following groups: *oceanic mantle peridotites*, *arc-related peridotites*, and *continental peridotite xenoliths*. This classification scheme is not perfect as it may introduce artificial distinctions when there may be none. The grouping of these subdivisions is made to provide a means of assessing V correlation with tectonic environment, as proposed earlier by Canil (1999, 2002).

Massif peridotites (Lanzo, Italy; French Pyrenees; NE Pyrenees; Ronda massif, Spain) and abyssal peridotites (peridotites derived from fracture zones in the seafloor) are categorized here as *oceanic mantle peridotites*. The classification of massif peridotites as oceanic mantle peridotites relies on the assumption that such peridotites are the residues of mid-ocean ridge basalts. Alternatively, they may be residues of basalts formed in back-arc spreading centers, in which case it is possible that they may have been formed or influenced by subduction-related processes. We will revisit this issue in the discussion.

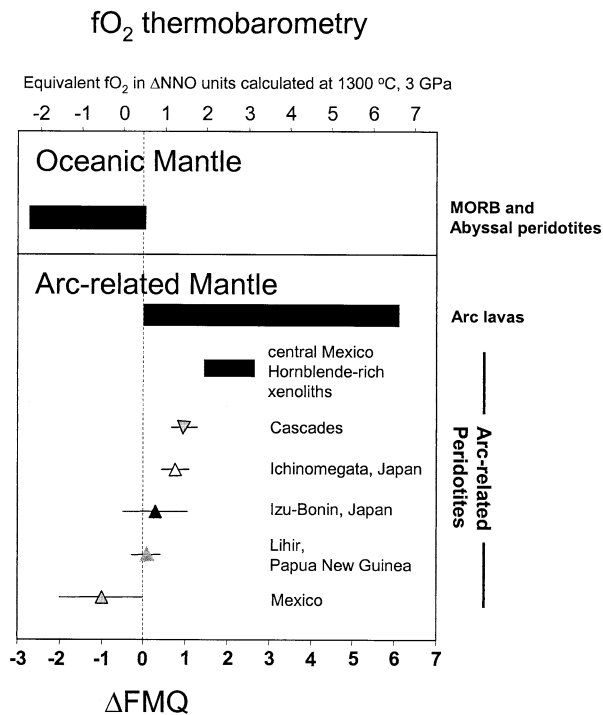Peridotite xenoliths erupted in volcanic centers related to arc

Fig. 1. Range in fO_2 in log unit deviations from the quartz-fayalite-magnetite buffer (FMQ). Peridotite fO_2's are based on Fe^{3+}/Fe^{2+} distribution in mineral phases: Cascades (Brandon and Draper, 1996), Izu Bonin fore-arc (Parkinson and Pearce, 1998), Ichinomegata in Japan (Wood and Virgo, 1989), the Mexican arc (Luhr and Aranda-Gomez, 1997; Lattard, 2001), and Lihir in the Papua New Guinea arc (McInnes et al., 2001). Also shown is the range for hornblende-rich peridotite xenoliths from central Mexico (Blatter and Carmichael, 1998). The fields for arc lavas and midocean ridge basalts are based on Fe^{3+}/Fe^{2+} ratios of lavas (Christie et al., 1986; Wooden and Miller, 1990; Carmichael, 1991). Equivalent fO_2's expressed in log-unit deviations from the Ni-NiO buffer are shown at the top of the diagram (calculated at 1300°C and 3 GPa).

magmatism are classified as *arc-related peridotites*. Included in this group are certain seafloor-dredged peridotites, which are in close proximity to present-day arcs (e.g., Izu-Bonin fore-arc). All remaining peridotite xenoliths found in continentally emplaced volcanic centers that are not obviously associated with present-day arc magmatism are categorized as *continental peridotite xenoliths*. This classification scheme makes no assumption on whether continental lithospheric mantle was formed in an arc environment or mid-ocean ridge environment.

Intrinsic oxygen fugacities determined by oxygen thermobarometry (based on the Fe^{3+} activity of melts, Kress and Carmichael, 1991, or the Fe^{3+} activity of various mineral phases, Ballhaus et al., 1990) are shown in Figure 1, where oxygen thermobarometric measurements between oceanic mantle peridotites and arc-related peridotites and lavas are compared (Christie et al., 1986; Wood and Virgo, 1989; Ballhaus et al., 1990; Wood et al., 1990; Carmichael, 1991; Ballhaus, 1995; Brandon and Draper, 1996; Blatter and Carmichael, 1998; Parkinson and Arculus, 1999; McInnes et al., 2001). Arc-related peridotites and arc lavas have higher thermobarometric fO_2's than oceanic mantle peridotites and mid-ocean ridge basalts.

It is important to reiterate that thermobarometric fO_2 (defined

by the Fe^{3+} activity in peridotite minerals) defines the fO_2 imposed by the *last* equilibration event, which in the case of mantle xenoliths, does not necessarily reflect the conditions under which melting occurred because the system could have been open to O_2 exchange after the primary partial melting event. It is therefore not necessary that thermobarometric fO_2 and the fO_2 inferred from V systematics coincide.

2.2. Assessment of Interlaboratory Bias

Measurements are mostly by X-ray fluorescence (XRF) or inductively coupled plasma mass spectrometry (ICP-MS). Only the data of Fabries et al. (1989) represent atomic absorption data. In using literature compilations, interlaboratory bias must be assessed. However, this was difficult to do because standard data are not always published in the literature. The new V concentrations presented in this study (measured by XRF and ICP-MS) on basalt standard BHVO-1 agree within error of measurements made by three other XRF laboratories responsible for some of the literature data used here (301 ± 16 ppm, 1 S.D., n = 5). From this database, only three laboratories published XRF analyses of a peridotite standard (DTS-1); the relative standard deviation of this small group was 10% (12 ± 1 ppm). These estimates of interlaboratory bias, while incomplete, are consistent with a blind comparison of a dolerite (340 ppm V) and gabbro (189 ppm V) interlaboratory standard between 104 XRF laboratories (Govindaraju et al., 1994), yielding V measurements agreeing to within 10% for each standard (1 S. D.). These uncertainties should be considered the best-case scenario insofar as the foregoing provides only a reasonable assessment of interlaboratory bias.

As standard data were not available with every set of literature data used here, the worst-case scenario for interlaboratory bias was thus estimated by comparing data for oceanic mantle peridotites (massif and abyssal peridotites) determined by different laboratories (Fig. 2). It is implicitly assumed that the V systematics of all oceanic peridotites are identical, that is, all of these peridotites partially melted under identical fO_2 conditions, have identical initial compositions, and have minimal metasomatic disturbance of V. With these assumptions, the entire spread in V data (±10 ppm) then reflects the worst-case scenario for interlaboratory bias (dashed lines in Figs. 2B,C). Clearly, some of the differences between data sets are likely to be real, so the true uncertainty is likely to be bracketed by the above two estimates of uncertainty.

2.3. Partial Melting Calculations

2.3.1. Partial Melting at 1.5 GPa

Vanadium abundances in peridotites were modeled as a function of the degree of melting (F) and fO_2. These models use experimental calibrations of crystal-liquid partition coefficients as a function of fO_2 and melting stoichiometries determined from experiments or thermodynamic considerations. The thermodynamic-based program pMELTS was used to calculate isobaric anhydrous partial melting paths at 1.5 GPa (Ghiorso and Sack, 1995; Asimow and Ghiorso, 1998), while experimental calibrations were used to calculate the isobaric anhydrous melting paths at 3.0 and 7.0 GPa. The use of a thermodynamic approach to model melting stoichiometry at 1.5 GPa
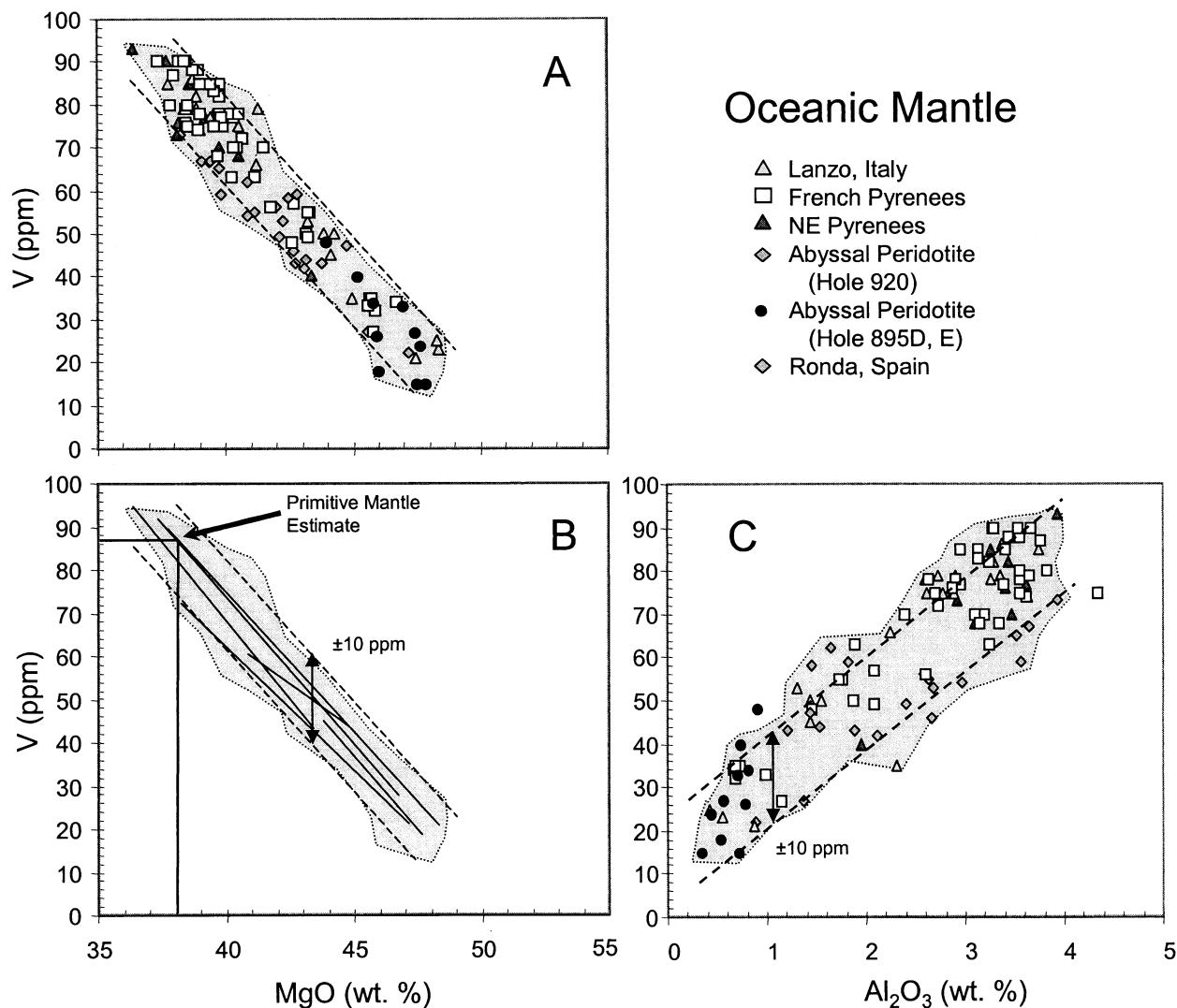
Fig. 2. (A) V-MgO of abyssal peridotites and obducted massif or ophiolitic peridotites assumed to represent oceanic mantle (Frey et al., 1985; Suen and Frey, 1987; Bodinier, 1988; Bodinier et al., 1988; Fabries et al., 1989; Burnham et al., 1998). V and major-element data for Hole 920 are shown in the Appendix and in (Brandon et al., 2000), respectively. Total region covered by the data has been shaded in gray. Primitive mantle V is estimated to be ~87 ppm based on extrapolation of the regression line for all data to 38 wt% MgO (pyrolite composition from McDonough and Sun, 1995). Pair of dashed lines is taken as a worst-case scenario for interlaboratory bias (±10 ppm V), assuming that each group of peridotites partially melted under identical fO_2 conditions. (B) Individual regressions for each peridotite suite shown in (A) (data points are excluded for clarity). (C) Same as (A), but data are expressed in V-Al_2O_3 space.

differs from the experimentally based approach used by Canil (2002). The 3.0 and 7.0 GPa melting models rely on partial melting experiments of Walter (1999), which is the same approach taken by Canil (2002). We explored the thermodynamic-based approach at 1.5 GPa to consider the effects of closed system behavior of O_2 on V partitioning, that is, fO_2 was allowed to vary with F depending on how Fe^{3+} is distributed amongst mineral phases. Polybaric melting more likely reflects the true melting path in the mantle, but the pressure range over which residual peridotites melted is unknown, and therefore, no attempt to model polybaric melting was made. As a first step, V systematics resulting from isobaric melting, where the model parameters in the calculations are better understood, are investigated in this paper.

For the pMELTS calculations, the initial major-element composition of the peridotite was adjusted from McDonough and Sun's (1995) estimate of primitive upper mantle by assuming no K_2O and by slightly increasing the SiO_2 content to match the slightly higher SiO_2 content of some of the peridotites considered in this study. The starting composition was thus 45.5 wt% SiO_2, 4.3 wt% Al_2O_3 and 37.5 wt% MgO. The initial V abundance (87 ppm) was determined by extrapolating the oceanic peridotite data array (Fig. 1) to 37.5 wt% MgO (McDonough and Sun, 1995) and is within error of McDonough and Sun's estimate of 82 ppm for the primitive upper mantle.

Using the pMELTS program, the melting stoichiometry and major-element composition of the residue at 1.5 GPa was calculated for anhydrous peridotite for the following condi-

tions: equilibrium melting at buffered fO_2 (a system open to O_2 exchange), fractional melting at buffered fO_2, and fractional melting in a system closed to O_2 exchange. The degree of melting was controlled by incrementally increasing the temperature. For fractional melting, melts were incrementally extracted at 20°C intervals. The major-element composition of the residue and the melting stoichiometry as a function of F were not significantly different between fractional and equilibrium melting (although the relationship between F and temperature was different), so the modeled major-element compositions and modal mineralogies of the residues assume equilibrium melting (Table 1). For fractional melting in a system closed to O_2, the bulk-rock Fe^{3+}/Fe^{2+} ratio was pre-equilibrated to a given fO_2 and the bulk-rock fO_2 was then allowed to evolve with progressive melting. Due to changes in the proportions of minerals and melt (and temperature) with progressive melting, the activity of Fe^{3+} in the various mineral phases changes during melting, resulting in a change in fO_2. There were no significant differences between the melting stoichiometries at different fO_2's.

Vanadium abundances were modeled assuming fractional melting. In this model, fractional melting was implemented by incremental equilibrium melting (increments of 20°C) using the following equation:

$$C_s^{j+1} = D^{j+1}C_s^j / \{D(1 - \Delta F^{j+1}) + \Delta F^{j+1}\} \quad (1)$$

where ΔF is the $(j + 1)$th incremental fraction of melt extracted from the system, D is the bulk partition coefficient ($D^{j+1} = \Sigma X_i^{j+1}D_i$, where X_i^{j+1} and D_i are the mineral modes and crystal/liquid partition coefficients at the $j + 1$ increment), C_s^j is the abundance of V in the bulk rock before extraction of the $(j + 1)$th melt increment. The crystal/liquid partition coefficients were adopted from the series of experimental studies conducted by Canil (2002 and references therein). For clinopyroxene, olivine and spinel, the crystal/liquid partition coefficients were calculated using the following empirical relationship (Canil, 2002):

$$D = a/(10^{b\Delta NNO + c} + 1) \quad (2)$$

where $a = 8$, $b = 0.31$, and $c = 1.22$ for clinopyroxene, $a = 0.9$, $b = 0.31$, and $c = 1.53$ for olivine, $a = 18.5$, $b = 0.37$ and $c = 0.62$ for spinel, and $\Delta NNO = \log_{10}(fO_2) - \log_{10}(fO_2^{NNO})$, where NNO represents the Ni-NiO oxygen buffer. For orthopyroxene, the relationship (Canil, 2002), $D_{opx} = ce^{b\Delta NNO}$, was used ($b = -0.215$, $c = 0.116$). These functional relationships are shown graphically in Figure 3.

Oxygen fugacities were expressed as the logarithm deviation from the fayalite-magnetite-quartz buffer $\Delta FMQ = \log_{10}(fO_2) - \log_{10}(fO_2^{FMQ})$. Conversion from ΔFMQ to ΔNNO was determined using the following empirical relationship (Frost, 1991):

$$\log fO_2 = A/T + B + C(P - 1)/T \quad (3)$$

where $A = -24930$, $B = 9.36$, $C = 0.046$ for the NNO buffer, and $A = -25096.3$, $B = 8.735$, $C = 0.110$ for the FMQ buffer ($T =$ Kelvin, $p =$ bar).
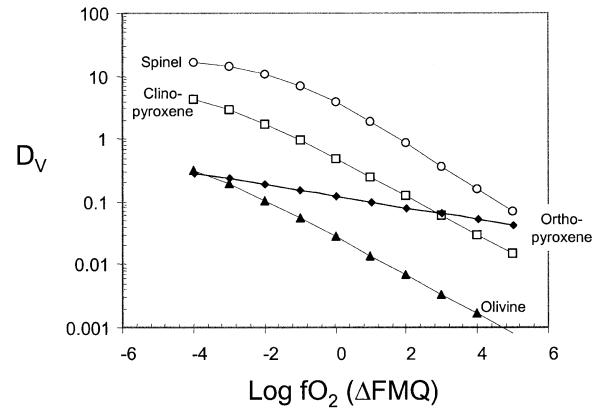

Fig. 3. Mineral/melt partition functions as a function of fO_2 (expressed in delta log units from the fayalite-quartz-magnetite buffer). Parameterizations are taken from Canil (1997, 1999, 2002) and Canil and Fedortchouk (2000, 2001).

2.3.2. Partial Melting at 3 and 7 GPa

The major element composition and melting stoichiometries as a function of degree of melting at 3.0 and 7.0 GPa (Table 1) were determined from the results of high pressure equilibrium-melting experiments of dry fertile garnet peridotite (Walter, 1998, 1999). The starting composition of the 3.0 and 7.0 GPa experimental studies was slightly less silicic (45.0 wt% SiO_2) than the starting composition used in the 1.5 GPa melting calculations discussed above (45.5 wt% SiO_2). There was no attempt to modify the starting composition for the 3.0 and 7.0 GPa melting models to fit the more silicic nature of some peridotites because these high pressure models were constrained by the experiments. However, the initial Al_2O_3 and MgO contents used for both melting models were identical. For the 3.0 and 7.0 GPa melting models, it is also assumed that the differences in melting stoichiometry between fractional and equilibrium melting and between high fO_2 and low fO_2 melting are small. As in Canil (2002), the garnet/liquid partition coefficient was assumed to be 1. The V content of the bulk residue was calculated assuming fractional melting as described above.

3. RESULTS

3.1. Post-Archean Peridotites

Figure 4 shows V-MgO and V-Al_2O_3 data for post-Archean spinel peridotites, subdivided into the following categories: oceanic mantle, arc-related peridotites, and continental peridotite xenoliths. The oceanic mantle peridotite array from Figure 2 is reproduced in each figure (gray shading) to facilitate comparisons between the different subdivisions. Also plotted are fO_2-buffered V-MgO melting curves at 1.5 GPa between FMQ $- 3$ and FMQ $+ 2$ at 1 log unit increments (solid lines); the bold line represents the FMQ-buffered partial melting path. Ten percent melting increments are shown as vertical dashed lines; increased melt extraction results in an increase in MgO and decrease in Al_2O_3 in the peridotite residue. The negative slopes of the V-MgO melting curves and the positive slopes of the V-Al_2O_3 melting curves reflect the moderate incompatibility of V during melting (Fig. 3). The depletion of V is predicted
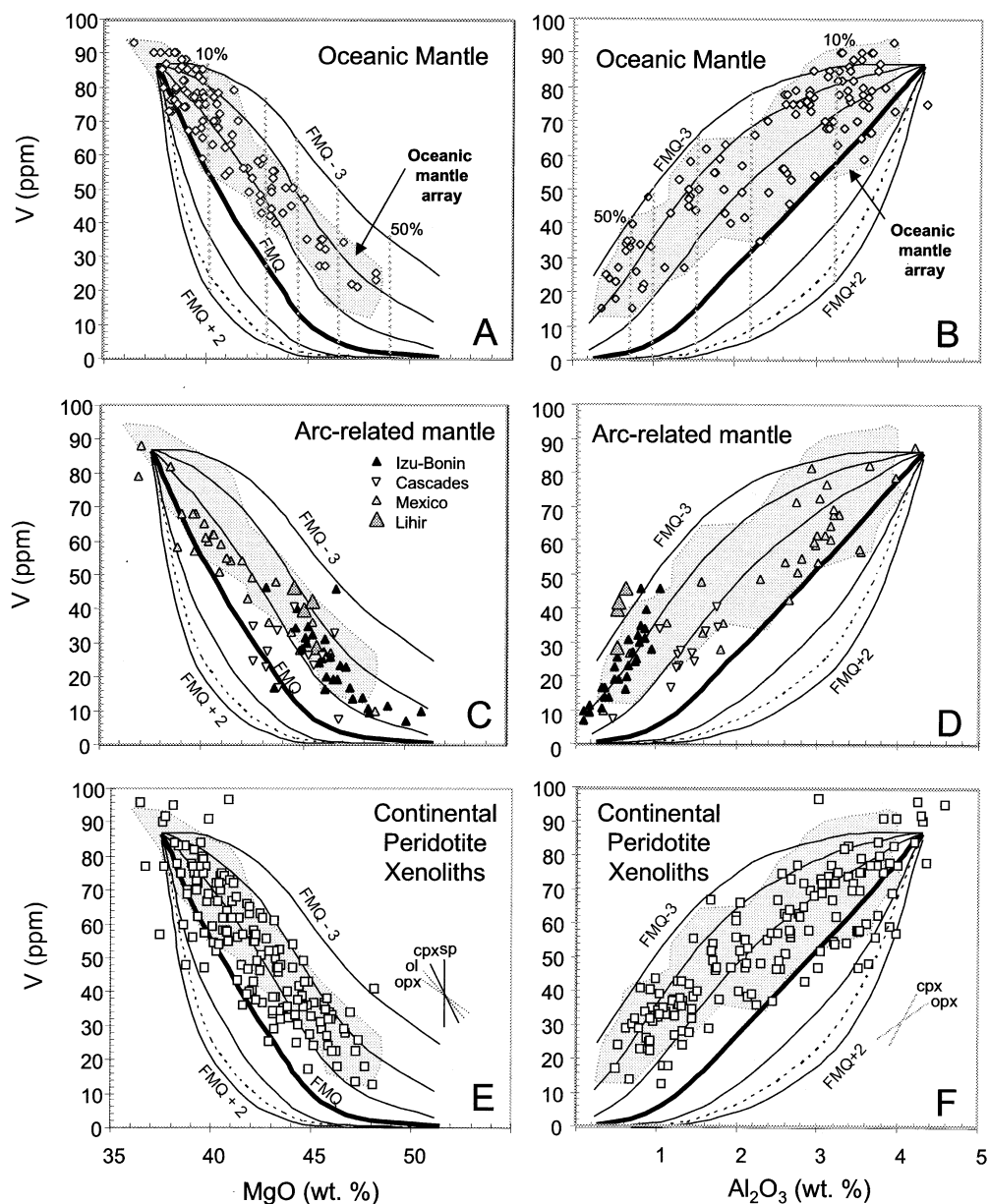
POST-ARCHEAN PERIDOTITES

Fig. 4. Vanadium, MgO and Al_2O_3 contents of post-Archean oceanic mantle peridotites (A, B), arc-related peridotites (C, D), and continental peridotite xenoliths (E, F). Partitioning is modeled using parameterizations shown in Figure 3. In all figures, the range of oceanic mantle peridotites is denoted by the gray shaded region as shown in Figure 2A. Data for oceanic mantle are from references listed in the caption to Figure 2. Arc-related peridotite data are from (Luhr and Aranda-Gomez, 1997; Parkinson and Pearce, 1998; Gregoire et al., 2001; Lee, 2001; McInnes et al., 2001) or data presented in the Appendix (Cascades). Peridotite xenoliths from lavas erupted through post-Archean continental crust are from (Frey and Green, 1974; Dupuy et al., 1986; Stolz and Davies, 1988; Yaxley et al., 1991; Qu et al., 1995; Vaselli et al., 1995; Bedini et al., 1997; Zangana et al., 1999) or from the Appendix. Solid curves in all figures represent 1.5 GPa, fO_2-*buffered* partial melting curves with a starting composition having an approximately pyrolitic major-element composition and 87 ppm V. Partial melting curves are at 1 log unit intervals, spanning fO_2's from FMQ − 3 to FMQ + 2 (thick solid line represents FMQ). Dashed lines in all figures represent the unbuffered fractional melting case in which fO_2 is initially prescribed to be FMQ but allowed to evolve with progressive melting in a system closed to O_2 exchange. The evolution of fO_2 with degree of melting is shown in Figure 5. Dotted vertical lines represent the degree of melt extracted in 10% increments.

to be greater at high fO_2 due to the increased incompatibility of V as fO_2 increases (Fig. 3).

It can be seen that oceanic mantle peridotites (Figs. 4A,B)

largely fall between the FMQ and FMQ − 3 melting curves in V-MgO and V-Al_2O_3 space. The fact that massif peridotites plot in the same field as the abyssal peridotites suggests that our

Table 1. Composition of residues (wt%).

1.5 GPa melting—pMELTS

F %	MgO	Al_2O_3	SiO_2	opx	cpx	ol	sp
0	37.5	4.3	45.5	28.1	19.2	49.6	3.1
1.0	37.8	4.2	45.5	28.3	18.9	49.8	3.0
2.4	38.1	4.0	45.5	28.4	18.3	50.3	3.0
5.0	38.7	3.7	45.5	28.8	17.0	51.4	2.8
9.9	39.8	3.2	45.6	30.2	13.5	53.8	2.5
18.3	41.9	2.4	45.6	34.4	5.0	58.6	1.9
24.9	43.6	1.8	45.5	35.5	0	62.9	1.6
30.3	44.6	1.4	45.2	32.1		66.5	1.3
37.1	46.0	1.1	44.6	27.0		71.9	1.2
46.6	48.0	0.7	43.4	17.8		81.2	1.0

3 GPa melting—Walter (1998)

F %	MgO	Al_2O_3	SiO_2	opx	cpx	ol	gt
0	37.5	4.3	45.0	17.4	26.2	52.3	4.1
2.5	38.1	4.1	44.9	18.5	24.5	54.0	3.1
5.0	38.6	3.8	44.8	19.5	22.8	55.7	2.1
7.5	39.2	3.6	44.7	20.6	21.0	57.4	1.1
10.0	39.8	3.4	44.6	21.7	19.2	59.1	0
12.5	40.3	3.1	44.5	22.5	17.2	60.3	
15.0	40.9	2.9	44.4	23.4	15.2	61.4	
17.5	41.4	2.6	44.3	25.0	10.4	64.5	
20.0	42.0	2.4	44.2	28.9	5.2	65.9	
22.5	42.8	2.1	44.1	32.2	0	67.8	
25.0	43.5	1.9	43.9	33.8		66.2	
27.5	44.3	1.6	43.8	30.6		69.4	
30.0	45.0	1.3	43.6	27.4		72.6	
32.5	45.8	1.0	43.5	24.1		75.9	
35.0	46.5	0.8	43.3	20.8		79.2	
37.5	47.3	0.5	43.2	17.4		82.6	
40.0	48.0	0.2	43.0	13.9		86.1	
42.5	48.8	0.0	42.8	10.4		89.6	
45.0	49.5		42.5	7.0		93.0	
47.5	50.3		42.3	3.5		96.5	
50.0	51.0		42.0	0		100	

7 GPa Melting—Walter (1998)

F %	MgO	Al_2O_3	SiO_2	opx	cpx	ol	gt
0	37.5	4.3	45.0		29.7	53.5	16.8
2.5	37.8	4.3	45.0		29.4	54.0	16.7
5.0	38.1	4.2	45.0		29.1	54.4	16.5
7.5	38.4	4.2	45.0		28.8	54.9	16.3
10.0	38.8	4.1	45.0		28.5	55.4	16.1
12.5	39.1	4.1	45.0		28.1	55.9	15.9
15.0	39.4	4.0	45.0		27.8	56.4	15.8
17.5	39.7	4.0	45.0		27.5	56.9	15.6
20.0	40.0	3.9	45.0		27.2	57.4	15.4
22.5	40.5	3.8	44.9		26.0	58.8	15.2
25.0	41.0	3.7	44.7		24.9	60.2	15.0
27.5	41.5	3.6	44.6		23.7	61.5	14.8
30.0	42.0	3.5	44.4		22.5	62.9	14.6
32.5	42.5	3.3	44.3		21.4	64.3	14.4
35.0	43.0	3.2	44.1		20.2	65.7	14.1
37.5	43.5	3.1	44.0	0	15.7	70.9	13.4
40.0	44.0	3.0	43.8	5.1	10.3	72.6	12.0
42.5	44.6	2.8	43.6	10.1	5.0	74.3	10.6
45.0	45.3	2.5	43.4	14.9	0	75.9	9.2
47.5	45.9	2.3	43.1	18.6	0	73.9	7.6
50.0	46.5	2.0	42.9	15.2	0	78.2	6.6

4A and B. Higher fO_2's are predicted when the V-MgO melting curves are used in conjunction with the oceanic mantle data. This feature of the model results from our assumed Al_2O_3 starting composition, which is slightly higher than the highest Al_2O_3 contents of the oceanic mantle peridotites. If the Al_2O_3 starting composition is assumed to be 3.8 wt% instead of 4.3 wt%, the curves in Figures 4B, D, and F would shift to the left by approximately 0.5 wt%, eliminating the discrepancy.

Regardless of this discrepancy, at high degrees of melting (e.g., >30 wt% melt extracted; Figs. 4A,B), the oceanic mantle peridotites have V-MgO and V-Al_2O_3 systematics that fall mainly between the FMQ − 1 and FMQ − 3 melting curves. At low degrees of melting, the V data fall between the FMQ + 1 and FMQ − 3 melting curves (some data even fall above the FMQ − 3 curve). This apparent increased range in fO_2 at low degrees of melting is an artifact of the limited "resolution" of the melting curves at low degrees of melting due to the limited range in V-MgO-Al_2O_3 variance for changing fO_2 in the models. The fO_2 range inferred from the V-MgO systematics at moderate to high degrees of melting (FMQ − 3 to FMQ − 1) is consistent with "thermobarometric fO_2" of oceanic mantle as determined from the distribution of Fe^{3+}/Fe^{2+} in peridotitic minerals or the Fe^{3+}/Fe^{2+} of mid-ocean ridge basalt glasses (Fig. 1).

The range of arc-related peridotites in V-MgO and V-Al_2O_3 space (Fig. 4C,D) overlaps considerably with that of the oceanic mantle peridotites (Fig. 4A,B), but a small proportion of arc-related peridotites (some Cascades and Izu Bonin xenoliths) appear to have slightly lower V contents for a given MgO or Al_2O_3 content. Although these differences are small, they are distinguishable from the worst-case estimate of interlaboratory bias (straight dashed lines in Fig. 2B,C). Examining the data at moderate to high degrees of melting, it can be seen that arc-related peridotites as a whole fall between the FMQ and FMQ − 3 melting curves. This is consistent with the inferred fO_2's of melting in arc-related peridotites, largely coinciding with those of oceanic mantle peridotites (FMQ − 3 to FMQ − 1). Some Cascade and Izu-Bonin xenoliths may extend the range to subtly higher fO_2's (e.g., FMQ). This range in paleo-fO_2 (FMQ − 3 to FMQ) falls well within the range of thermobarometric fO_2's determined from Fe^{3+}/Fe^{2+} ratios in arc-related peridotitic minerals (FMQ − 2 to FMQ + 3). Intriguingly, they fall in the lower end of thermobarometrically determined fO_2's (Fig. 1) on arc-related peridotites and lavas (FMQ − 2 to FMQ + 4). For example, the V data for the Cascades xenoliths imply fO_2's of melting (FMQ − 1 to FMQ) only slightly higher than that of oceanic mantle (Fig. 4C,D), but the thermobarometrically determined fO_2's on the same Cascade xenoliths are much higher (FMQ to FMQ + 2) as shown in Figure 1.

The majority of V-MgO and V-Al_2O_3 data for continental peridotite xenoliths plot between FMQ + 1 and FMQ − 3, so their V systematics are indistinguishable from oceanic and arc-related mantle.

3.1.1. Fractional Melting in a System Closed to O_2 Exchange

The V-MgO and V-Al_2O_3 evolution during partial melting at 1.5 GPa in a system closed to O_2 exchange was also modeled.

classification scheme for oceanic mantle peridotites is robust. There appears to be a slight discrepancy between the fO_2's inferred from the V-MgO and V-Al_2O_3 systematics in Figures
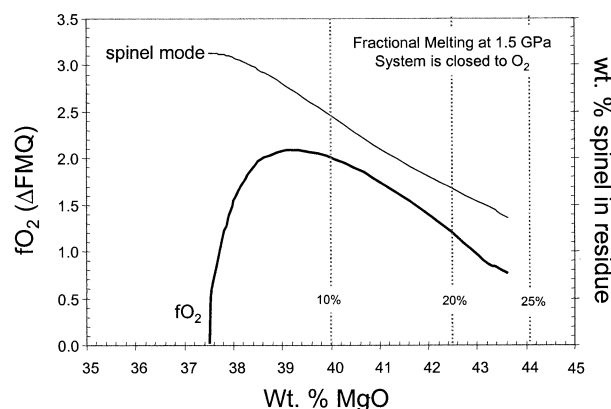
Fig. 5. The evolution of fO_2 in a 1.5 GPa system undergoing fractional melting in a system closed to O_2 exchange using the pMELTS thermodynamically based modeling program described in the text (represented by the dashed V-MgO and V-Al$_2$O$_3$ melting curves in Fig. 4). Also shown is the variation in the spinel mode (wt% in residue) as a function of the degree of melting. Vertical dotted lines represent 10% increments in degree of melt extracted.

In this model, the combined O_2 content of the melts and solid residue remains constant. The fO_2 of the system is free to change after an initial fO_2 equivalent to the FMQ buffer is prescribed (dashed curve in Fig. 4). The fO_2 of the solid residue and melt at each fraction of melt extracted is equal. However, with each fraction of melt extracted, the fO_2 of the residual peridotite is updated according to changes in the phase proportions with increasing degree of melting. The closed-system evolution of fO_2 as a function of degree of melting (using MgO as a proxy) is shown in Figure 5 (bold line). It can be seen that although the peridotite begins with a fO_2 equal to FMQ, the fO_2 rises very quickly to nearly FMQ + 2 as melting proceeds. This results in a very rapid depletion of V during partial melting, as can be seen by comparing the dashed lines for melting in O_2-closed systems to the thick solid lines (fO_2-buffered) in Figure 4. The increase in fO_2 is due to the redistribution of Fe^{3+} and Fe^{2+} among solid phases as phase proportions and temperature change with degree of melting. It can be seen in Figure 5 that the spinel mode in the residue decreases with increasing degrees of melting (thin line). The increase in fO_2 can be explained by the fact that spinel is the dominant Fe^{3+}-bearing mineral phase in the peridotite residue and therefore, a decrease in spinel mode is accompanied by an increase in Fe^{3+} activity in the spinel, which essentially defines the fO_2 of the peridotite residue. The fO_2 of the peridotite residue then dictates the activity of Fe^{3+} in the next fraction of melt generated from this residue.

The fO_2 evolution path shown in Figure 5 is extremely model-dependent. The calculations presented here assume a dry peridotite system. In the presence of volatile species (e.g., CO_2, CH_4, H_2O, SO_2), the fO_2 evolution path will undoubtedly be different (Ballhaus and Frost, 1994), but such calculations are beyond the scope of this paper. However, regardless of how realistic the pMELTS fO_2 melting path is, any increase in fO_2 of the residue-melt system during partial melting will result in rapid depletion of V, which is not observed in the V-MgO systematics of any post-Archean peridotites.

3.1.2. Archean Peridotites

Figure 6 shows the V-MgO systematics of Archean peridotites from Tanzania (Fig. 6E,F), South Africa (Fig. 6A,B), and Siberia (Fig. 6C,D). Buffered-fO_2 (FMQ − 4 to FMQ + 2) melting curves at 3 GPa are shown in Figures 6A, C, and E and at 7 GPa in Figures 6B, D, and F. The V-Al$_2$O$_3$ systematics are presented in Figure 7. All Archean peridotites have equilibration pressures between 2.5 and 5 GPa based on mineral thermobarometry, but partial melting models at 7 GPa were considered to entertain the possibility that the original partial melting event may have occurred at pressures higher than the current equilibration pressures (Walter, 1999).

The peridotites from the South African and Siberian cratons (Figs. 6A–D) are subdivided into high temperature (HTP; gray circles) and low temperature peridotites (LTP; black circles). HTPs are characterized by sheared porphyroclastic textures, equilibration temperatures (>1350°C) exceeding typical lithospheric geotherm temperatures, slightly more fertile major element compositions (higher FeO, CaO and Al$_2$O$_3$), and minerals showing complex chemical zonation (Nixon and Boyd, 1973). LTPs are characterized by equilibration pressures and temperatures that typically fall on predicted conductive geotherms, more refractory major-element compositions (lower FeO, CaO, and Al$_2$O$_3$, higher MgO), equilibrium mineral textures and fabric (equigranular), and minerals that are chemically unzoned (Nixon and Boyd, 1973). It is generally believed that the HTPs are anomalous samples of the deep lithosphere or the asthenosphere (Nixon and Boyd, 1973), but their petrogenetic origin remains uncertain. One possible hypothesis is that the HTPs represent original refractory lithospheric mantle peridotites (e.g., LTPs), which have been refertilized by basaltic melt infiltration shortly before eruption of the host kimberlite because of the preservation of disequilibrium textures and mineral chemistries (e.g., Smith and Boyd, 1992). The HTPs are plotted in Figure 6 for completeness, but omitted in Figure 7 for clarity.

Overall, the 3 GPa melting curves (Figs. 6A,C,E and 7B) are similar to the 1.5 GPa melting curves (Figs. 4 and 7A), the former involving garnet in the residue and the latter involving spinel in the residue. In detail, however, V appears to be more rapidly depleted during 3 GPa melting than during 1.5 GPa melting (compare Fig. 7A with Fig. 7B). This is attributed to early exhaustion of garnet during melting at 3 GPa, whereas spinel persists as a residual mineral throughout partial melting at 1.5 GPa. The 7 GPa melting curves (e.g., Fig. 6B) differ distinctly from the 1.5 and 3 GPa melting curves in that V is depleted even less rapidly. This is attributed to the higher bulk compatibility of V imposed by the large amount of garnet in the residue at 7 GPa melting, particularly at low to moderate degrees of partial melting.

Figures 6E,F and 7C show that Tanzanian cratonic peridotites (open circles) plot as an extension of the post-Archean oceanic mantle peridotite array in V-MgO and V-Al$_2$O$_3$ space. The Tanzanian data fall between the FMQ − 2 and FMQ − 4 partial melting curves for both 3 and 7 GPa.

In V-MgO space, the South African LTPs (black circles in Figs. 6A,B) form an elongate region, which diverges from the V-depleted end of the post-Archean oceanic mantle array along a trajectory that plots distinctly below the post-Archean oceanic
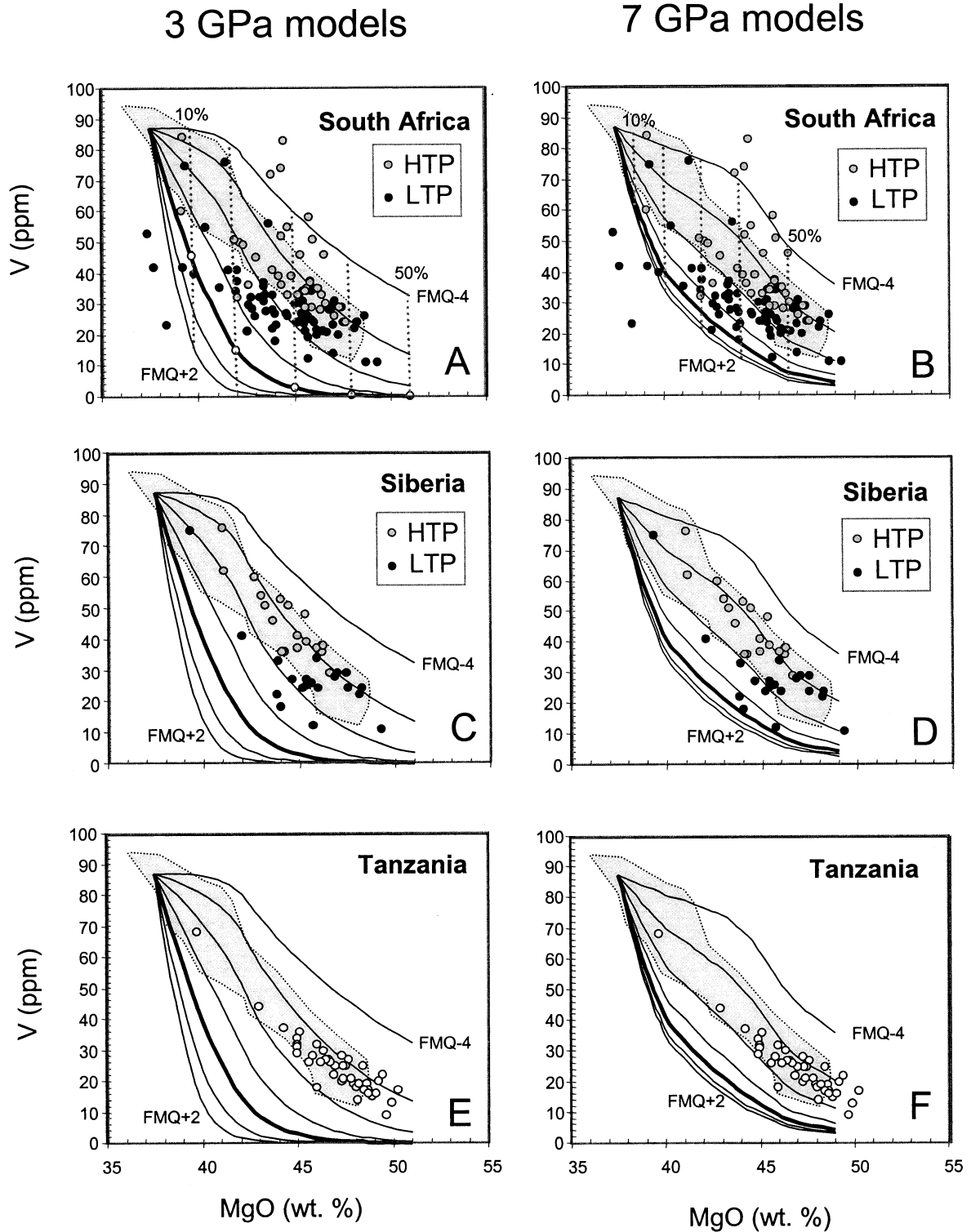
3 GPa models

7 GPa models

Fig. 6. Vanadium and MgO contents of Archean cratonic peridotites. (A, B) South African cratonic peridotites (Boyd and Mertzman, 1987; Boyd, 1989; McDonough and Frey, 1989; Winterburn et al., 1989; Boyd et al., 1998). (C, D) Siberian craton (Boyd et al., 1997). (E, F) Tanzanian cratonic peridotites (Rudnick et al., 1994; Lee and Rudnick, 1999; Lee, 2001). For South African (A, B) and Siberian peridotites (C, D), gray circles represent high temperature sheared peridotites (HTPs) and black circles represent low temperature sheared peridotites (LTPs). Left-hand panels (A, C, E) and right-hand panels (B, D, F) depict 3 and 7 GPa fO_2-buffered melting curves, respectively. Melting curves range from FMQ $-$ 4 to FMQ $+$ 2 at 1 log unit intervals. Bold solid line represents partial melting at FMQ. Arrowed trajectories represent approximate mixing trajectory with orthopyroxene in equilibrium with a primitive magma (see text for discussion).
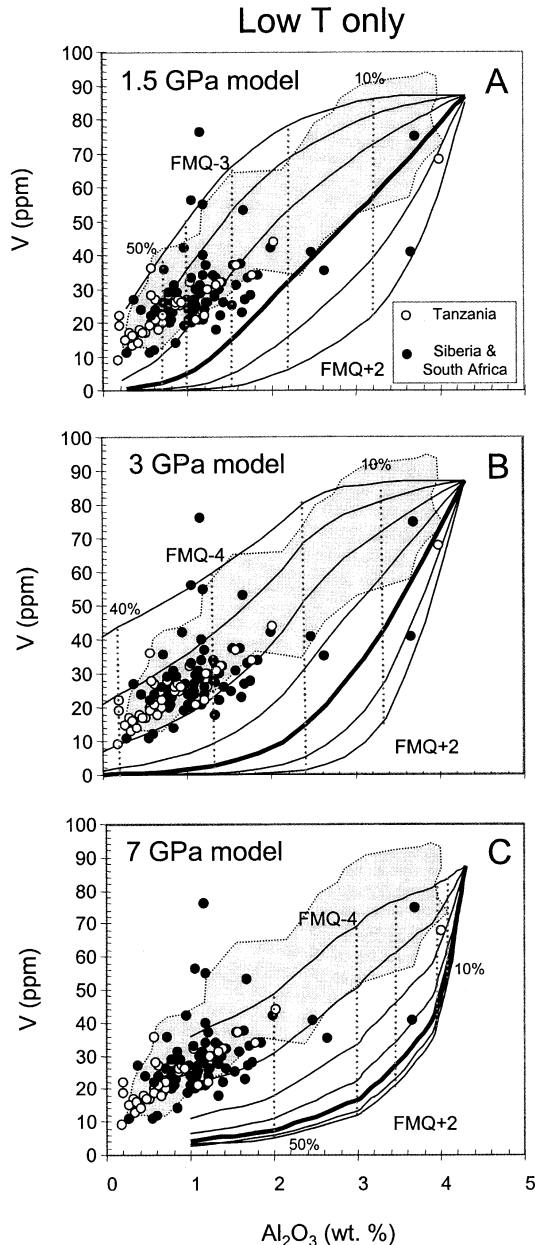
Fig. 7. Vanadium and Al_2O_3 contents of Archean peridotites. High temperature peridotites (HTPs) have been eliminated for clarity. South African and Siberian low temperature peridotites (LTPs) have been grouped together. Arrows represent hypothetical orthopyroxene mixing trajectories as discussed in the text.

mantle array. A smaller divergence from the oceanic mantle array is also seen in V-Al_2O_3 space (Fig. 7). Although the South African LTPs plot between the FMQ − 4 and FMQ + 1 partial melting curves for both 3 and 7 GPa, the data array appears to obliquely crosscut the fO_2-buffered partial melting curves. The majority of the HTPs plot within the oceanic mantle array although some plot well above the array. The V systematics of the HTPs, taken at face value, imply melting between FMQ − 1 and FMQ − 4 using the 3 and 7 GPa

melting curves. The samples with very high V might imply partial melting at very low fO_2 (e.g., <FMQ − 4). However, given the pervasive evidence for refertilization processes in HTPs (Boyd, 1987), it is possible that the anomalously high V contents of some HTPs are due to the addition of ultramafic melts characterized by high V contents (>100 ppm V). The origin of the HTPs remains uncertain and is not discussed any further in this paper.

The Siberian LTPs appear to coincide with the lower extension of the post-Archean oceanic mantle array, but some samples also plot distinctly below the oceanic mantle array akin to many of the South African LTPs. These V-MgO and V-Al_2O_3 data lie between the FMQ − 4 and FMQ − 2 partial melting curves at 3 GPa and the FMQ − 4 and FMQ curves at 7 GPa. The Siberian HTPs plot on an array that almost exactly coincides with the oceanic mantle array, un-like the South African HTPs.

4. DISCUSSION

4.1. Prospects and Limitations of V as a Proxy for Paleo-fO_2 Determination

The sensitivity of V partitioning during melting of a peridotite has already been demonstrated by Canil and coworkers in a series of studies based on experiments and global compilations of V data (Canil, 1997, 1999, 2002; Canil and Fedortchouk, 2000, 2001). However, the applicability of these partial melting experiments to real samples is limited by a number of uncertainties.

The first uncertainty is interlaboratory bias. Here, the worst- and best-case scenarios for interlaboratory bias were estimated, allowing an assessment of the limitations of using V as a proxy for paleo-fO_2 during melting. The worst-case scenario (±10 ppm V) was estimated by taking the spread of oceanic mantle peridotite data in V-MgO space and assuming that all oceanic mantle peridotite suites formed under identical conditions. Some of the differences in the V-MgO systematics between arc-related peridotites, oceanic mantle peridotites, and Archean peridotites are larger than the worst-case estimates of interlaboratory bias (Figs. 2 and 4), confirming that V data are precise enough to track differences in partial melting fO_2 (provided modal metasomatism did not overprint the V contents). The degree to which relative differences in fO_2 can be inferred from V systematics can be estimated by comparing the worst-case scenario interlaboratory bias (dashed lines in Figs. 2B,C) with the fO_2-buffered partial melting models. The resolution of the V-MgO partial melting curves between FMQ and FMQ − 3 (Figs. 4, 6, and 7) shows that ~1 log unit differences in fO_2 are resolvable in the case of spinel-facies melting (e.g., 1.5 GPa, Fig. 4) and ~0.5 log unit differences are resolvable in the case of garnet-facies melting (Figs. 6 and 7). The fO_2-resolution of the melting curves decreases considerably at fO_2's higher than ~FMQ + 1 because V is effectively removed from peridotite residues at highly oxidizing conditions. This is shown by the compaction of V-MgO fO_2-isopleths for fO_2's >FMQ + 1 for 1.5 GPa melting and >~FMQ for 3 and 7 GPa melting (Figs. 4 and 6).

Additional factors that should be considered in estimating absolute fO_2 are uncertainties in the starting composition and

the melting stoichiometry, the latter dependent on the pressure (or pressures) at which melting takes place. Each of these issues are discussed in turn. In regards to estimating the starting composition, it can be seen from Figures 4, 6, and 7 that small changes in the initial major element composition of the un-melted peridotite can cause the modeled melting curves to shift laterally. For example, as already pointed out in Section 3, assuming a starting composition with a slightly lower Al content will shift the fO_2-melting curves towards the left to better coincide with the fO_2-curves in V-MgO space. An inspection of Figures 4, 6, and 7 suggests that an additional 1 log-unit uncertainty in fO_2 is introduced if the starting composition is not precisely known.

Canil (2002) pointed out that the pressure or pressures over which melting occurred is not tightly constrained, so it is not exactly clear which group of partial melting models should be used to compare real V data. For partial melting in the spinel peridotite facies (~1–2 GPa), the melting stoichiometry does not change significantly over the pressure interval in which spinel is stable. Hence the 1.5 GPa V-MgO melting curves shown in Figure 4 provide a fairly robust representation of spinel facies melting with no significant uncertainty in the fO_2 isopleths. For partial melting in the garnet stability field, the large differences in melting stoichiometry between 3 and 7 GPa are clearly evident in both the shapes of the V-MgO melting curves and the rate at which V is depleted for a given fO_2. This introduces an additional uncertainty in the fO_2 curves of 1 log unit for this pressure range (defined by the garnet facies).

Additional uncertainties in determining absolute and relative fO_2's from V-MgO systematics arise from sample heterogeneity, the possibility of non-buffered fO_2 during melting, the effects of polybaric melting, and metasomatic effects. As V is largely concentrated in spinels, the combination of small sample size and coarse mineral grain size could yield fractionations in V-MgO and V-Al_2O_3 systematics. Approximate mixing vectors for various peridotitic minerals are shown in Figure 4. The calculated buffered fO_2 melting paths illustrated in Figures 4 and 6 are an ideal situation. It is not clear if partial melting at buffered-fO_2 is realistic. Nevertheless, it was shown in Section 3 that, regardless of uncertainties in modeling parameters, any large (e.g., 2 log units) increases in fO_2 during melting would result in rapid V depletion, which is not seen in any of the peridotite V data.

While uncertainties in the modeling may restrict quantification of fO_2 to ±1 log unit, a relative, qualitative evaluation of fO_2 among different suites is limited only by analytical uncertainty (~±0.5 log unit). In other words, peridotite suites can be ordered in a relative fO_2 sequence based on their V contents at a given MgO or Al_2O_3 content to a better precision than can be quantified by the models.

4.2. Similarity in fO_2 of Melting in Subarc Mantle and beneath Midocean Ridges

Some peridotites from the mantle overlying modern subduction zones (some Cascades and Izu Bonin samples) have slightly lower V contents for a given MgO and Al_2O_3 content compared to samples from the oceanic mantle (Fig. 4C,D). This is consistent with partial melting at fO_2's that are up to ~1 log unit higher than in oceanic mantle. However, the majority of
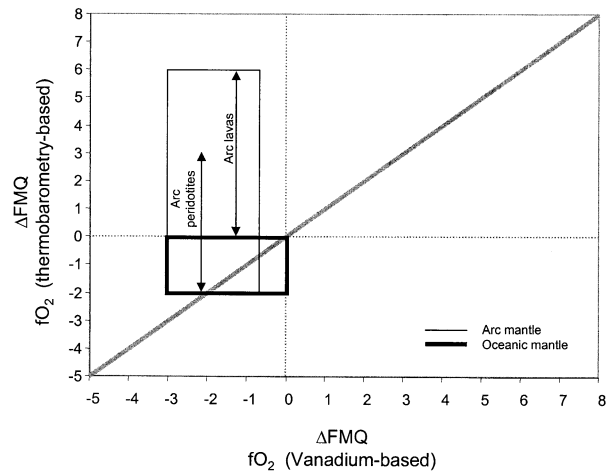

Fig. 8. Comparison of thermobarometric fO_2's determined by Fe^{3+} activity in spinel or melts (Fig. 1) compared to fO_2's of melting determined by V data. The field for arc lavas are based on Fe^{3+}/Fe^{2+} ratios of lavas (Carmichael, 1991). Axes are plotted in log-unit deviations from the fayalite-quartz-magnetite buffer. Diagonal line represents the 1:1 correspondence.

arc-related peridotites in Figure 4C,D have V systematics indistinguishable from those derived from oceanic mantle. The conclusion can be drawn that the V contents of arc-related peridotites are consistent with partial melting at fO_2's as high as FMQ but down to fO_2's as low as FMQ − 3. Oceanic mantle peridotites have V contents indicating melting between FMQ − 1 and FMQ − 3. Thus, arc-related peridotites appear to have undergone partial melting at a range of fO_2's from conditions similar to oceanic mantle to ~FMQ. Such fO_2's inferred from V data fall within the lower end of thermobarometrically determined fO_2's of arc-related peridotites and lavas (Figs. 1 and 8; FMQ − 2 to FMQ + 6).

If partial melting occurred at fO_2's as high as implied by some of the thermobarometrically determined fO_2's (up to FMQ + 2), the V contents of arc peridotites should be more depleted than observed for a given MgO or Al_2O_3 content (Fig. 4). Although some of the arc-related peridotites examined in this study have slightly lower V contents than oceanic mantle peridotites, none of the examined arc-related peridotites exhibit the extent of V depletion expected for the high fO_2's implied by fO_2-thermobarometry. Thus, if V systematics retain the fO_2 conditions during partial melting, then melting within the sub-arc mantle wedge primarily occurs at fO_2's similar to melting beneath mid-ocean ridges.

This conclusion raises a dilemma. Thermobarometric fO_2's of arc-related peridotites indicate that these rocks last equilibrated at very high fO_2's in contrast to the V systematics, which indicate that partial melting in the mantle wedge occurred at low fO_2's, similar to oceanic mantle (Fig. 8). As thermobarometric fO_2's, calculated using the Fe^{3+} activities in mineral phases, reflect the most recent equilibration conditions, they record fO_2's that postdate the fO_2 set during partial melting (Brandon and Draper, 1996, 1998). The decoupling between thermobarometric fO_2 and partial melting fO_2 inferred from V systematics is a result of metasomatic overprinting that affects the activity of Fe^{3+} in minerals more than the bulk V in these

peridotites. This has important ramifications for the interpretation of the Archean data presented below.

4.3. What Was the fO_2 of Archean Mantle?

4.3.1. Disturbance of V Systematics in Some Archean Peridotites

The V-MgO and V-Al_2O_3 contents of the Archean Tanzanian cratonic peridotites fall primarily between the FMQ − 3 and FMQ − 2 melting curves (Figs. 6E,F and 7). In contrast, the LTP South African and Siberian peridotites have more scattered V systematics. Many have lower V contents for a given MgO and Al_2O_3 than those that plot within the field of post-Archean oceanic mantle, and plot correspondingly on high-fO_2 melting curves. These systematics were taken at face value by Canil to be consistent with partial melting at high fO_2's and may indicate an origin in an arc environment (Canil, 1999, 2002).

An alternative explanation for the V-MgO-Al_2O_3 systematics of the Siberian and South African LTPs warrants discussion. It has been previously shown that a number of South African and Siberian cratonic peridotites have had secondary orthopyroxene likely added through one or more of the following processes: metamorphic differentiation, cumulate processes, and melt-rock reaction (Boyd, 1989; Rudnick et al., 1994; Kelemen et al., 1998; Herzberg, 1999; Walter, 1999). Although these modal metasomatic processes occurred after partial melting, it is important to clarify that these processes differ distinctly from the metasomatic processes responsible for generating the HTPs. The LTPs are in textural and chemical equilibrium whereas the HTPs show pervasive evidence for disequilibrium, indicating that the metasomatic processes responsible for orthopyroxene-enrichment occurred long ago and are hence a long-term feature of cratonic lithospheric mantle, while the HTPs represent a very recent episode of metasomatism.

The addition of orthopyroxene results in Si-enrichment of the peridotite because of the high Si content of pyroxenes compared to other peridotitic minerals. The Tanzanian peridotites, by contrast, do not appear to show evidence for pervasive orthopyroxene enrichment (Lee and Rudnick, 1999). In Figure 9, V versus SiO_2 is plotted for Archean peridotites and post-Archean oceanic mantle peridotites. Isobaric, fO_2-buffered partial melting curves at 1.5 and 3 GPa are shown for reference. The V-SiO_2 systematics of the majority of oceanic mantle peridotites and all of the Archean Tanzanian cratonic peridotites can be easily explained by partial melting of an approximately pyrolitic-type source (although a slightly higher SiO_2 content (1–2 wt%) is required (Fig. 9). In contrast, many South African and Siberian LTPs have anomalously high SiO_2 (or equivalently excess orthopyroxene), forming a distinct array in V-SiO_2 space that diverges from the partial melting trends (Fig. 9). The anomalous SiO_2, resulting from excess orthopyroxene, cannot be modeled by partial melting unless a significantly more silicic starting material (~50 wt%) is assumed that far exceeds estimates for fertile mantle compositions.

Two end-member hypotheses have been suggested for the formation of excess orthopyroxene. In one hypothesis, orthopyroxene-rich cumulates from a high pressure, mafic to ultramafic
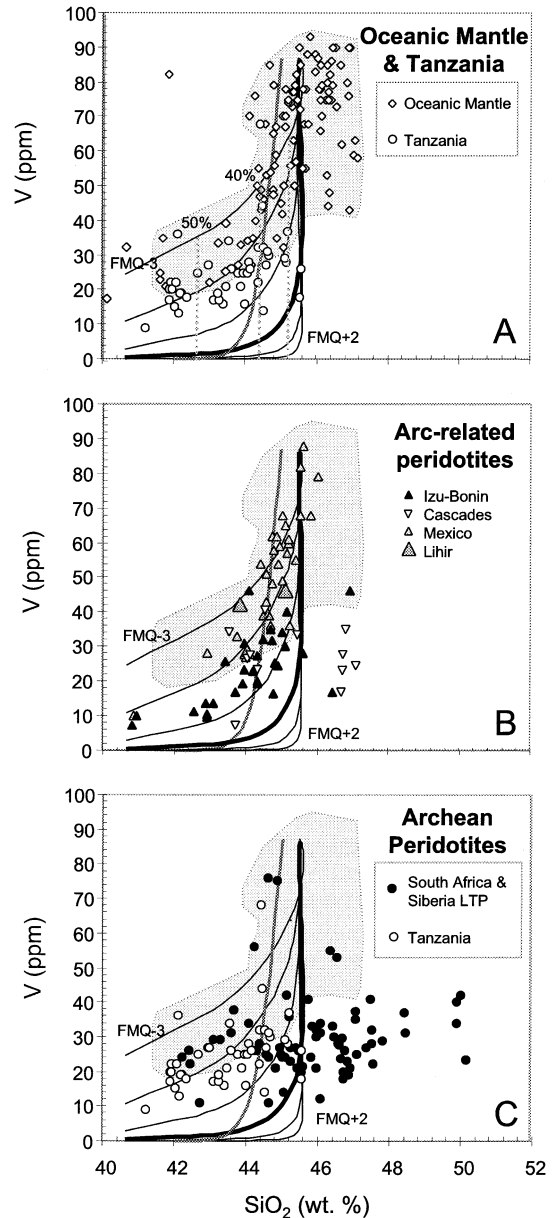

Fig. 9. Vanadium and SiO_2 contents of Archean cratonic peridotites (circles), post-Archean oceanic mantle peridotites (diamonds), and arc-related peridotites (triangles). Archean Tanzanian peridotites are represented by open circles. South African and Siberian low temperature peridotites are represented by solid symbols. High temperature peridotites are not shown. Buffered-fO_2 melting curves at 1.5 GPa are shown as thin solid lines; lines represent 1 log unit intervals ranging from FMQ − 3 to FMQ + 2. Thick solid line represents the 3 GPa melting curve at fO_2 = FMQ. The 3 GPa melting curve is based on parameters derived from experimental studies, which use starting compositions with slightly lower SiO_2 contents than the typical fertile post-Archean oceanic mantle peridotite. No attempt was made to change the experimental starting composition. In the case of the 1.5 GPa melting curves, a thermodynamic-based approach was taken so the starting composition was easily modified.

magma chamber mechanically mix with residual harzburgite, driving the harzburgite to orthopyroxene-rich compositions (Herzberg, 1999). The other hypothesis is that a Si-rich melt or
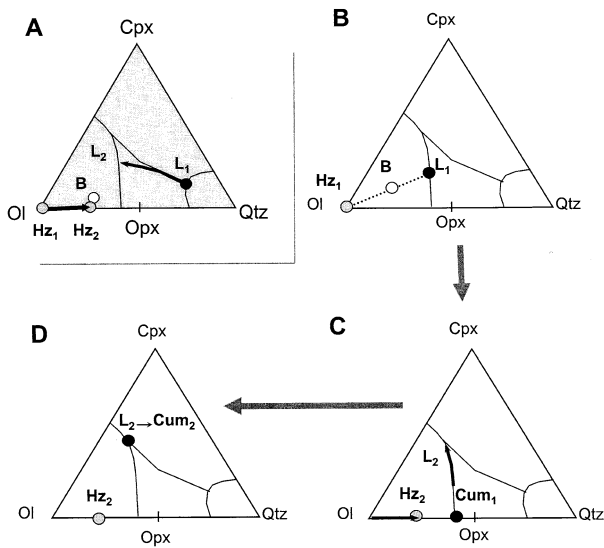
Fig. 10. Normative pseudoternary phase diagrams at ~3 GPa (projected from the Al-phase), which schematically illustrate the concepts of melt rock reaction (A) and addition of orthopyroxene-rich cumulates to residual harzburgite (B–D) (Kelemen, 1995; Kelemen et al., 1998). In both scenarios, Hz_1 represents the initially unreacted orthopyroxene-poor residual harzburgite. Hz_2 represents the final composition of the peridotite after melt-rock reaction (A) or cumulate addition (B–D). During melt-rock reaction, a silicic melt L_1 reacts with Hz_1 to generate Hz_2 and L_2. In the cumulate scenario, a melt L_1 originally in equilibrium with Hz_1 separates from Hz_1 to form a magma chamber. Upon cooling, cumulates of composition Cum_1 will crystallize, driving the melt towards L_2. The cumulates sink and mechanically mix with Hz_1 in the solid state, driving the bulk composition of the solid towards Hz 2.

fluid reacts with a residual harzburgite, generating orthopyroxene at the expense of olivine (Rudnick et al., 1994; Kelemen et al., 1998). This reaction could have taken place within the mantle wedge overlying a subduction zone during Archean times when the temperatures in the subducting slab could have been hot enough to partially melt eclogitized oceanic crust to generate Si-rich melts in the mantle (Kelemen et al., 1998). Each of these hypotheses are discussed below.

4.3.2. Melt-Rock Reaction Modeling

The easiest way to generate excess orthopyroxene in a harzburgite is to react it with a silicic melt. The effect of this reaction can be modeled by determining the equilibrium phase proportions and compositions in a system with a given melt/rock ratio. This concept is schematically illustrated in Figure 10. A highly melt-depleted residue (e.g., an orthopyroxene-poor harzburgite, Hz_1), mixes with a silicic melt, L_1, in proportions such that the new bulk composition is given by B. Assuming that this system is at equilibrium, the predicted phase proportions and compositions are denoted by the new equilibrium melt composition, L_2, and the new equilibrium harzburgite composition, Hz_2. It can be seen that the reaction of a silicic melt with olivine generates orthopyroxene, thereby driving the bulk composition of the harzburgite towards the orthopyroxene end member, resulting in silica enrichment.

A simple model of melt-rock reaction that can predict the

degree of orthopyroxene enrichment and concomitant changes in V content as a function of melt/rock ratio is explored. To do so, two simplifying assumptions are made. First, it is assumed that the harzburgite consists of only orthopyroxene and olivine because garnet and clinopyroxene are very scarce in most cratonic mantle harzburgites and because it has been suggested that the small amounts of garnet and clinopyroxene may actually represent subsolidus exsolution products from high temperature orthopyroxenes that can have a few wt% CaO and Al_2O_3 (Cox et al., 1987; Canil, 1992). Second, the amount of Al_2O_3 and CaO in the harzburgites is assumed to be small (consistent with the scarcity of garnet and clinopyroxene) and that, although the infiltrating melt has several wt% Al_2O_3 and CaO, melt-rock reaction is assumed to only generate excess orthopyroxene and not clinopyroxene or garnet (Fig. 10). Any amount of CaO and Al_2O_3 added to the harzburgite is taken up in the orthopyroxene. The change in solid phase proportions due to melt-rock reaction is modeled using mass action and mass balance equations, which assume exchange of only MgO, FeO and SiO_2 between the solids and the melt. As CaO and Al_2O_3 in the solid are small, this simplification is probably a good approximation to the change in modal mineralogy. Accordingly, the predicted SiO_2 contents of harzburgites undergoing melt-rock reaction are robust because there is very little substitution of other cations besides Si in the tetrahedral sites of orthopyroxene. However, the predicted MgO and FeO contents of the harzburgite during melt-rock reaction are overestimated because the incorporation of CaO and Al_2O_3 from the melt into orthopyroxene is ignored in this first-order approach. Therefore, to correct the MgO contents of the orthopyroxenes, we assumed that magmatic orthopyroxenes can have ~4 wt% Al_2O_3 and ~2 wt% CaO (Walter, 1999). Due to these assumptions, the modeled bulk MgO content (in contrast to the bulk SiO_2) of the reacting harzburgite represents a very rough approximation.

The above assumptions are expressed in the following equations. Mass balance of the chemical components (in wt%) requires

$$C_{total,i} = \sum_j C_{i,j}X_j \qquad (4)$$

where $C_{i,j}$ is the concentration of the ith oxide (MgO, FeO, SiO_2) in the jth phase (orthopyroxene, olivine, melt), X_j is the weight fraction of the jth phase, and $C_{total,i}$ is the concentration of the ith element in the entire melt + harzburgite system. The concentration sum of the remaining elements in the melt (e.g., CaO and Al_2O_3) is simply denoted by F_{melt}:

$$F_{melt} = 100 - \sum_i C_{i,melt} \qquad (5)$$

The concentrations of SiO_2, MgO, and FeO in the solid residue must sum to 100 wt%, that is,

$$100 = \frac{1}{1 - X_{melt}} \sum_j \sum_i C_{i,j}X_j \text{ for } j \neq melt \qquad (6)$$

where X^o_{melt} represents the original fraction of melt added, which is in general slightly different from the equilibrium melt fraction X_{melt} (e.g., melt can be either consumed or generated).

An empirical orthopyroxene-olivine distribution coefficient determined from cratonic harzburgites from Tanzania (Lee and Rudnick, 1999) is assumed:

$$C_{SiO_2,melt} = 100 - F(X^o_{melt}/X_{melt}) - C_{FeO,melt} - C_{MgO,melt}$$

$$(7)$$

$$\frac{C_{MgO,Ol}/C_{MgO,Opx}}{C_{FeO,Ol}/C_{FeO,Opx}} = 0.90 \qquad (8)$$

To relate mineral compositions to the melt, an effective MgO partition coefficient between olivine and melt based on the compilations in Jones (1995) is assumed. In doing so, D_{MgO} ($C_{MgO,Ol}/C_{MgO,melt}$) is set to 6.3 (intermediate between andesitic and basaltic liquids because the reacting melt is assumed to be silicic). The following relationship from Jones is used to relate the FeO and MgO contents of olivine:

$$D_{FeO} = 0.298 D_{MgO} + 0.27 \qquad (9)$$

Finally, the SiO_2 contents of orthopyroxene and olivine are fixed at 56 and 40 wt%, respectively. The MgO and FeO contents of orthopyroxene and olivine are determined from the above mass action laws and mineral stoichiometry.

Given the above discussions and the constraint that $\sum_j X_j = 1$, the entire system of unknowns simplifies to seven independent unknowns and seven non-linear equations. A Newton-Raphson iterative root-finding algorithm is used to solve the system of non-linear equations for the following unknowns: X_{Opx}, X_{melt}, $C_{MgO,Ol}$, $C_{MgO,Opx}$, $C_{FeO,Ol}$, $C_{FeO,Opx}$, C_{SiO2},melt. The V content of the peridotite was determined by proportioning the V in the bulk system among the various phases according to appropriate crystal/melt partition coefficients. For an andesitic melt composition, we assumed that the crystal/melt partition coefficient of V for orthopyroxene and olivine are ~1.10 and ~0.080 (Rollinson, 1993). These partition coefficients are slightly higher than those in basaltic systems.

The composition of the reacting silica-rich melt was taken to be that of a slab-derived melt (i.e., a partial melt of eclogitized oceanic crust), whose composition was determined from the average of experimental partial melts of eclogitized basalt at 3.2 and 3.8 GPa (Rapp et al., 1999): FeO = 3.1 wt%, MgO = 1.4 wt%, and SiO_2 = 67.5 wt%. For the initially unreacted orthopyroxene-poor harzburgite residue, a composition similar to the orthopyroxene-poor peridotites from Tanzania was assumed (FeO = 7.25, MgO = 44, SiO_2 = 48.75). The V concentration of the slab melt was estimated by assuming that the slab melt represents a 10% batch melt of basaltic eclogite. We assumed that the V concentration of basaltic eclogite before partial melting is given by the range (150 to 350 ppm V) seen in Archean basalts as shown in Figure 11 (picrites, which show olivine accumulation, are ignored). We also assumed that the basaltic eclogite is composed of a 1:1 ratio of garnet to clinopyroxene and that the V partition coefficients between these minerals and an andesitic melt was 8 for garnet and 1.1 for clinopyroxene, giving a bulk partition coefficient of 4.55 (based on compilations in Rollinson, 1993). The resulting V contents of partial melts of basaltic eclogite range from 35 to 83 ppm. Phanerozoic adakitic lavas, suggested by some investigators to be rare examples of recent slab-melting (Drummond et al., 1996), have an average V content of ~61 ppm, which falls
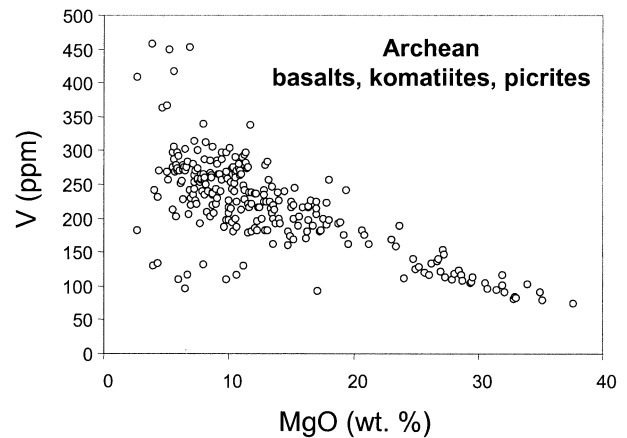

Fig. 11. Compilation of Archean basalts, komatiites and picrites from the literature. For the reaction models dicussed in the text, the V content of basalts is taken to lie between 150 and 350 ppm.

within our calculated range. We did not attempt to model the evolution of Al_2O_3 during melt-rock reaction.

In Figure 12, the V contents of South African and Siberian LTPs and Tanzanian peridotites are replotted as a function of SiO_2 and MgO. It can be seen that many of the South African and Siberian LTPs exhibit anomalously low V contents for a given MgO or SiO_2 content, forming shallow trajectories that deviate from the post-Archean oceanic mantle array (gray outlined region in Fig. 12). Superimposed on the data are the results of the melt-rock reaction modeling based on the assumptions outlined above. For each diagram, the compositional evolution of a harzburgite with increasing melt/rock ratio is shown for the addition of slab melts from oceanic crust with 150, 250, and 350 ppm V. Dashed lines represent the melt/rock ratio at 10% increments. The vertical bar represents the estimated V, MgO and SiO_2 content of an orthopyroxene in equilibrium with a basalt or ultramafic magma. It can be seen from the V-SiO_2 plot that the harzburgitic residue becomes nearly 100% orthopyroxene when the weight fraction of melt added to the system is ~0.8. The results of the modeling in V-MgO space are similar to that in V-SiO_2 space although there appears to be a slight discrepancy (by ~10 wt.% melt fraction) in the predicted melt fraction for a given data point. However, as discussed above, the predicted MgO content of orthopyroxenes depends on the amount of CaO and Al_2O_3 in the orthopyroxene and this is poorly constrained by the simplistic modeling approach presented here. The exact trajectory during melt-rock reaction in Figure 12 is sensitive to the starting compositions of the unreacted harzburgite and the slab melt and to the values of the V partition coefficients assumed. However, within these uncertainties, it can be seen that the V and major-element systematics of many of the South African and Siberian LTPs can be readily explained by melt-rock reaction.

4.3.3. Modeling of Cumulate Addition of Orthopyroxene

Simple mechanical addition of magmatic orthopyroxene can also explain the V-SiO_2 and V-MgO systematics of the orthopyroxene-rich harzburgites. This process is shown schematically in Figures 10B–D. An orthopyroxene-poor residual har-
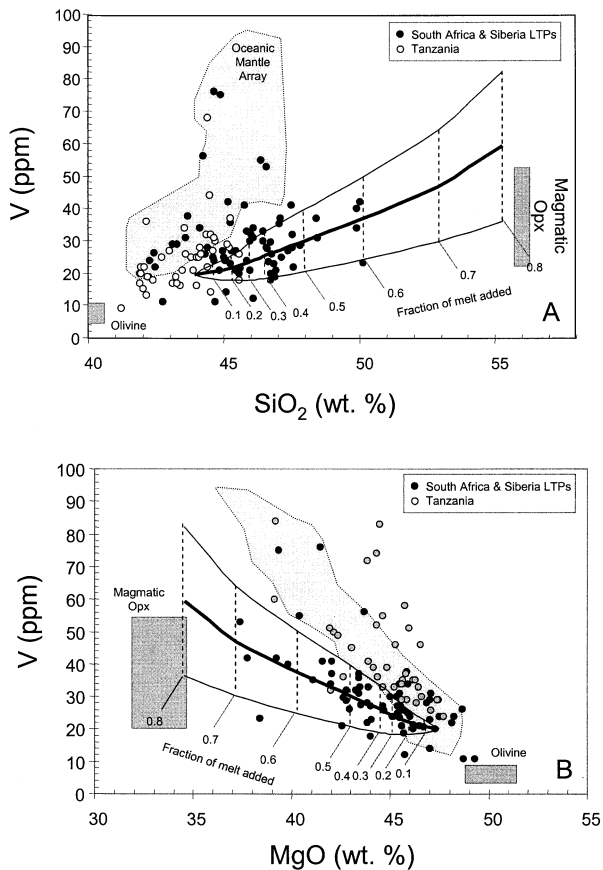
Fig. 12. V-SiO$_2$ (A) and V-MgO (B) diagrams showing Tanzanian peridotites (open circles) and LTPs from South Africa and Siberia (black circles). Gray outlined region represents the post-Archean oceanic mantle array. Curved lines represent the compositional evolution of the solid peridotite during melt rock reaction with increasing melt/rock ratio. The vertical dashed lines represent contours of 10% increments of melt added to the system. Each line corresponds to a different assumed V content of oceanic crust from which the silicic partial melt is generated. The bottom line corresponds to an oceanic crust having 150 ppm V, the middle line corresponds to 250 ppm V, and the upper line corresponds to 350 ppm V. Vertical gray bars (labeled "Magmatic Opx") represent the estimated V, MgO and SiO$_2$ content of magmatic orthopyroxene in basaltic systems as discussed in the text. Horizontal gray bars (labeled "Olivine") represent the predicted V contents of olivines in basaltic systems.

zburgite (Hz$_1$) is first in equilibrium with a mafic melt L$_1$ (Fig. 10B). The mafic melt is allowed to separate from the harzburgitic residue so that it crystallizes a nearly pure orthopyroxene cumulate (Cum$_1$) as shown in Figure 10C. This orthopyroxene-rich cumulate can mechanically mix with the orthopyroxene-poor residual harzburgite, driving the bulk composition of the solids towards more orthopyroxene-rich end members (e.g., Hz$_2$) as shown in Figure 10D.

In Figure 12, a hypothetical magmatic orthopyroxene end member is shown. This end-member composition is represented by an orthopyroxene in equilibrium with basaltic or ultramafic lavas (gray vertical bars in Fig. 12). The SiO$_2$ content of magmatic orthopyroxenes is more tightly constrained, whereas the MgO content of orthopyroxenes has higher variability owing to the variable amounts of CaO and

Al$_2$O$_3$ that may be incorporated in high temperature orthopyroxenes. The V content of the orthopyroxene end member was estimated using the partition coefficients of Canil at the FMQ buffer as shown in Figure 3 (Canil, 1997, 1999, 2002; Canil and Fedortchouk, 2000, 2001) and by assuming that the V content of the parental melt lies between 150 and 350 ppm (Fig. 11). In the cumulate mixing scenario, the composition of the cumulate will lie between the olivine and orthopyroxene end members in Figure 12 (olivine end member shown by horizontal gray bars). As the cumulate end member is nearly pure orthopyroxene, the mixing end member will lie close to the orthopyroxene end member (gray vertical bars). The V content of many of the South African and Siberian LTPs can be explained by mechanical mixing of an orthopyroxene-rich end member as well as by melt-rock reaction.

4.3.4. Similarity between Archean and Post-Archean V Systematics

In light of the above evidence for disturbance of V contents by orthopyroxene addition, there is no unequivocal support that cratonic mantle formed at fO_2's significantly higher than FMQ − 2. Although this does not preclude an arc origin for some Archean cratonic peridotites (because, as we have shown, there are no large differences between V systematics of arc and oceanic mantle peridotites), there is clearly no need to call upon an arc origin for cratonic peridotites from the V data alone. The Tanzanian peridotites, which appear to have escaped pervasive orthopyroxene enrichment, may reflect the precursor material of the Si-enriched South African and Siberian LTPs. If so, then cratonic mantle likely formed at fO_2's indistinguishable from post-Archean oceanic mantle. This conclusion contrasts with that of Canil (2002), who suggested many Archean peridotites could have formed at relatively oxidizing conditions.

4.4. Implications for the Evolution of Mantle fO_2

The above discussion suggests that middle to late Archean cratonic mantle formed at fO_2's similar to modern-day mantle (FMQ − 3 to FMQ). If the Earth's mantle was originally in equilibrium with the metallic core (e.g., O'Neill, 1991a,b), the mantle must have initially been at conditions reducing enough to stabilize metallic Fe (fO_2's must be less than that of the iron-wüstite buffer ∼ FMQ − 4). If the Archean cratonic peridotites are representative of the convecting mantle during this time, then the Earth's mantle was already oxidized to its present levels (FMQ − 3 to FMQ) by middle to late Archean times. Kump et al. (2001) proposed that the establishment of an oxygen-rich atmosphere ∼2.0 Ga ago was cuased by an increase in the fO_2 of the mantle by 2 log units. In agreement with Canil (2002), our analysis of V systematics shows that no increase in fO_2 of this magnitude is observed in the mantle 2.0 Ga ago. More recently, Holland (2002) has suggested that a much smaller increase in fO_2 (+0.5 log units) may be all that is needed to change the oxygen content of the atmosphere. This small change, however, is not resolvable by V systematics in ultramafic rocks.

5. CONCLUSIONS

The dependency of V partitioning on fO_2 makes V a potential recorder of paleo-fO_2 during partial melting. However, a

number of uncertainties limit the fO_2-resolving power of V data in peridotites. These limitations include interlaboratory bias in V data and uncertainties in the starting composition for partial melting models and in the pressure or pressures over which partial melting occurred. Despite these uncertainties, a number of conclusions can be made. Arc-related peridotites have V systematics very similar to oceanic mantle (FMQ − 3 to FMQ − 1), although some arc-related peridotites may have V systematics that imply partial melting at fO_2's of at most 1 log unit higher (e.g., FMQ). These findings imply that partial melting in the present-day mantle occurs at very similar fO_2's, regardless of tectonic environment. The lack of extremely high partial melting fO_2's in the subarc mantle wedge contrasts with the very high fO_2's determined thermobarometrically using the Fe^{3+} activities of mineral phases in some arc peridotites and arc lavas. This suggests that the fO_2's inferred from V systematics in peridotites are decoupled from the fO_2's determined from Fe^{3+} activities in peridotic minerals. It is concluded that V can retain a record of the fO_2 at the time of partial melting, whereas the Fe^{3+} activity of peridotitic minerals reflects a secondary fO_2 overprint associated with metasomatism.

Finally, it is shown that the V systematics of a number of late Archean peridotites have been disturbed by the addition of orthopyroxene through melt-rock reaction or cumulate processes. Orthopyroxene addition yields arrays with anomalously low V contents for a given degree of melting, resulting in the artifact of partial melting at high fO_2's. By correcting for orthopyroxene addition and by considering Archean peridotites unaffected by orthopyroxene addition (e.g., Tanzanian cratonic peridotites), it is concluded that late Archean cratonic mantle peridotites have V systematics no different from oceanic mantle today. There is neither any indication that late Archean cratonic mantle formed under highly oxidizing conditions characteristic of arc magmas or that such mantle formed at very reducing conditions. If the cratonic mantle suites studied here are representative of the whole mantle during late Archean times, it follows that the mantle must have achieved its oxidized state by late Archean times.

REFERENCES

Asimow P. D. and Ghiorso M. S. (1998) Algorithmic modifications extending MELTS to calculate subsolidus phase relations. *Am. Mineral.* **83,** 1127–1132.
Ballhaus C. (1995) Is the upper mantle metal-saturated? *Earth Planet. Sci. Lett.* **132,** 75–86.
Ballhaus C., Berry R. F., and Green D. H. (1990) Oxygen fugacity controls in the Earth's upper mantle. *Nature* **348,** 437–440.
Ballhaus C. and Frost B. R. (1994) The generation of oxidized CO_2-bearing basaltic melts from reduced CH_4-bearing upper mantle sources. *Geochim. Cosmochim. Acta* **58,** 4931–4940.

Bedini R. M., Bodinier J.-L., Dautria J. M., and Morten L. (1997) Evolution of LILE-enriched small melt fractions in the lithospheric mantle: A case study from the East African Rift. *Earth. Planet. Sci. Lett.* **153,** 67–83.
Blatter D. L. and Carmichael I. S. E. (1998) Hornblende peridotite xenoliths from central Mexico reveal the highly oxidized nature of subarc upper mantle. *Geology* **26,** 1035–1038.
Bodinier J.-L. (1988) Geochemistry and petrogenesis of the Lanzo peridotite body, western Alps. *Tectonophysics* **149,** 67–88.
Bodinier J.-L., Dupuy C., and Dostal J. (1988) Geochemistry and petrogenesis of eastern Pyrenean peridotites. *Geochim. Cosmochim. Acta* **52,** 2893–2907.
Boyd F. R. (1987) High- and low-temperature garnet peridotite xenoliths and their possible relation to the lithosphere-asthenosphere boundary beneath southern Africa. In *Mantle Xenoliths* (ed. P. H. Nixon), pp. 403–412. Wiley.
Boyd F. R. (1989) Compositional distinction between oceanic and cratonic lithosphere. *Earth Planet. Sci. Lett.* **96,** 15–26.
Boyd F. R. and Mertzman S. A. (1987) Composition and structure of the Kapvaal lithosphere, Southern Africa. In *Magmatic Processes: Physicochemical Principles: A Volume in Honor of Hatten S. Yoder, Jr.,* Vol. 1 (ed. B. O. Mysen), pp. 13–24. Geochemical Society Special Publication.
Boyd F. R., Pokhilenko N. P., Pearson D. G., Mertzman S. A., Sobolev N. V., and Finger L. W. (1997) Composition of the SIberian cratonic mantle: Evidence from Udachnaya peridotite xenoliths. *Contrib. Mineral. Petrol.* **128,** 228–246.
Boyd F. R., Pearson D. G., and Mertzman S. A. (1998) Spinel-facies peridotites from the Kaapvaal root (abstract). *Int. Kimb. Conf. Extended Abstr.* **7,** 100–102.
Brandon A. D. and Draper D. S. (1996) Constraints on the origin of the oxidation state of mantle overlying subduction zones: An example from Simcoe, Washington, USA. *Geochim. Cosmochim. Acta* **60,** 1739–1749.
Brandon A. D. and Draper D. S. (1998) Reply to the comment by B. R. Frost and C. Ballhaus on "Constraints on the origin of the oxidation state of mantle overlying subduction zones: An example from Simcoe, Washington, USA." *Geochim. Cosmochim. Acta* **62,** 333–335.
Brandon A. D., Snow J. E., Walker R. J., Morgan J. W., and Mock T. D. (2000) ^{190}Pt-^{186}Os and ^{187}Re-^{187}Os systematics of abyssal peridotites. *Earth Planet. Sci. Lett.* **177,** 319–335.
Burnham O. M., Rogers N. W., Pearson D. G., van Calsteren P. W., and Hawkesworth C. J. (1998) The petrogenesis of the eastern Pyrenean peridotites: An integrated study of their whole-rock geochemistry and Re-Os isotope composition. *Geochim. Cosmochim. Act.* **62,** 2293–2310.
Canil D. (1992) Orthopyroxene stability along the peridotite solidus and the origin of cratonic lithosphere beneath southern Africa. *Earth Planet. Sci. Lett.* **111,** 83–95.
Canil D. (1997) Vanadium partitioning and the oxidation state of Archaean komatiite magmas. *Nature* **389,** 842–845.
Canil D. (1999) Vanadium partitioning between orthopyroxene, spinel and silicate melt and the redox states of mantle source regions for primary magmas. *Geochim. Cosmochim. Acta* **63,** 557–572.
Canil D. (2002) Vanadium in peridotites, mantle redox and tectonic environments: Archean to present. *Earth. Planet. Sci. Lett.* **195,** 75–90.
Canil D. and Fedortchouk Y. (2000) Clinopyroxene-liquid partitioning for vanadium and the oxygen fugacity during formation of cratonic and oceanic mantle lithosphere. *J. Geophys. Res.* **105,** 26003–26016.
Canil D. and Fedortchouk Y. (2001) Olivine-liquid partitioning for vanadium and other trace elements with applications to modern and ancient picrites. *Can. Mineral.* **39,** 319–330.
Carmichael I. S. E. (1991) The redox states of basic and silicic magmas: A reflection of their source regions? *Contrib. Mineral. Petrol.* **106,** 129–141.
Chesley J. T., Rudnick R. L., and Lee C.-T. (1999) Re-Os systematics of mantle xenoliths from the East African Rift: Age, structure, and history of the Tanzanian craton. *Geochim. Cosmochim. Acta* **63,** 1203–1217.
Christie D. M., Carmichael I. S. E., and Langmuir C. H. (1986) Oxidation states of mid-ocean ridge basalt glasses. *Earth. Planet. Sci. Lett.* **79,** 397–411.

Cox K. G., Smith M. R., and Beswetherick S. (1987) Textural studies of garnet lherzolites: Evidence of exsolution origin from high-temperature harzburgites. In *Mantle Xenoliths* (ed. P. H. Nixon), pp. 537–550. Wiley.

Drummond M. S., Defant M. J., and Kepezhinskas P. K. (1996) Petrogenesis of slab-derived trondhjemite-tonalite-dacite/adakite magmas. *Trans. R. Soc. Edinburgh* **87**, 205–215.

Dupuy C., Dostal J., Dautria J. M., and Girod M. (1986) Geochemistry of spinel peridotite inclusions in basalts from Hoggar, Algeria. *J. Afr. Earth Sci.* **5**, 209–215.

Fabries J., Bodinier J.-L., Dupuy C., Lorand J.-P., and Benkerrou C. (1989) Evidence for modal metasomatism in the orogenic spinel lherzolite body from Caussou (northeastern Pyrenees, France). *J. Petrol.* **30**, 199–228.

Frey F. A. and Green D. H. (1974) The mineralogy, geochemistry and origin of lherzolite inclusions in Victorian basanites. *Geochim. Cosmochim. Acta* **38**, 1023–1059.

Frey F. A., Suen J. C., and Stockman H. W. (1985) The Ronda high temperature peridotite: Geochemistry and petrogenesis. *Geochim. Cosmochim. Acta* **49**, 2469–2491.

Frost R. B. (1991) Introduction to oxygen fugacity and its petrologic importance. In *Oxide Minerals: Petrologic and Magnetic Significance*, Vol. 25 (ed. D. H. Lindsley), pp. 1–9. Mineral. Soc. Am. Rev. Mineralogical Society of America.

Ghiorso M. S. and Sack R. O. (1995) Chemical mass transfer in magmatic processes. IV. A revised and internally consistent thermodynamic model for the interpolation and extrapolation of liquid-solid equilibria in magmatic systems at elevated temperatures and pressures. *Contrib. Mineral. Petrol.* **119**, 197–212.

Govindaraju K., Potts P. J., Webb P. C., and Watson J. S. (1994) 1994 report on Whin Sill dolerite WS-E from England and Pitscurrie microgabbro PM-S from Scotland: Assessment by one hundred and four international laboratories. *Geostand. News* **18**, 211–300.

Gregoire M., McInnes B. I. A., and O'Reilly S. Y. (2001) Hydrous metasomatism of oceanic sub-arc mantle, Lihir, Papua New Guinea, Part 2, Trace element characteristics of slab-derived fluids. *Lithos* **59**, 91–108.

Herzberg C. (1999) Phase equilibrium constraints on the formation of cratonic mantle. In *Mantle Petrology, Field Observations and High Pressure Experimentation: A Tribute to Francis R. (Joe) Boyd*, Vol. 6 (eds. Y. Fei, C. M. Bertka, and B. O. Mysen), pp. 241–257. Geochemical Society Special Publication.

Holland H. D. (1984) *The Chemical Evolution of the Atmosphere and Oceans.* Princeton University Press.

Holland H. D. (2002) Volcanic gases, black smokers, and the Great Oxidation Event, *Geochim. Cosmochim. Acta*, **66**, 3811–3826.

Jones J. H. (1995) Experimental trace element partitioning. In *Rock Physics and Phase Relations*, Vol. AGU Reference Shelf 3 (ed. T. J. Ahrens), pp. 73–104. American Geophysical Union.

Kasting J. F., Eggler D. H., and Raeburn S. P. (1993) Mantle redox evolution and the oxidation state of the Archean atmosphere. *J. Geol.* **101**, 245–257.

Kelemen P. B. (1995) Genesis of high Mg# andesites and the continental crust. *Contrib. Mineral. Petrol.* **120**, 1–19.

Kelemen P. B., Hart S. R., and Bernstein S. (1998) Silica enrichment in the continental upper mantle via melt/rock reaction. *Earth. Planet. Sci. Lett.* **164**, 387–406.

Kress V. C. and Carmichael I. S. E. (1991) The compressibility of silicate liquids containing Fe_2O_3 and the effect of composition, temperature, oxygen fugacity and pressure on their redox states. *Contrib. Mineral. Petrol.* **108**, 82–92.

Kump L. R., Kasting J. F., and Barley M. E. (2001) Rise of atmospheric oxygen and the "upside-down" Archean mantle. *Geochem. Geophys. Geosys.* **2**, 2000.GC000114.

Lattard D. (2001) Comment on "Mexican peridotite xenoliths and tectonic terranes: Correlations among vent location, texture, temperature, pressure, and oxygen fugacity" by J. F. Luhr and J. J. Aranda-Gomez. *J. Petrol.* **42**, 847–851.

Lee C.-T. (2001) The origin, evolution, and demise of continental lithospheric mantle: Perspectives from Re-Os isotopes, geochemistry, petrology, and modeling. Harvard University, PhD Thesis.

Lee C.-T. and Rudnick R. L. (1999) Compositionally stratified cratonic lithosphere: Petrology and geochemistry of peridotite xenoliths from

the Labait tuff cone, Tanzania. In Proc. VIIth International Kimberlite Conference, B. J. Dawson volume (eds. J. J. Gurney, J. L. Gurney, M. D. Pascoe, and S. R. Richardson), pp. 503–521.

Luhr J. F. and Aranda-Gomez J. J. (1997) Mexican peridotite xenoliths and tectonic terranes: Correlations among vent, location, texture, temperature, pressure, and oxygen fugacity. *J. Petrol.* **38**, 1075–1112.

McDonough W. F. and Frey F. A. (1989) Rare earth elements of upper mantle rocks. In *Geochemistry and Mineralogy of Rare Earth Elements*, Vol. 21 (eds. B. R. Lipin and G. McKay), pp. 99–145. Reviews in Mineralogy. Mineralogical Society of America.

McDonough W. F. and Sun S.-S. (1995) The composition of the Earth. *Chem. Geol.* **120**, 223–253.

McInnes B. I. A., Gregoire M., Binns R. A., Herzig P. M., and Hannington M. D. (2001) Hydrous metasomatism of oceanic sub-arc mantle, Lihir, Papua New Guinea: Petrology and geochemistry of fluid-metasomatised mantle wedge xenoliths. *Earth. Planet. Sci. Lett.* **188**, 169–183.

Nixon P. H. and Boyd F. R. (1973) Petrogenesis of the granular and sheared ultrabasic nodule suite in kimberlites. In *Lesotho Kimberlites* (ed. P. H. Nixon), pp. 48–56. Lesotho National Development Corporation.

O'Neill H. S. C. (1981) The transition between spinel lherzolite and garnet lherzolite, and its use as a geobarometer. *Contrib. Mineral. Petrol.* **77**, 185–194.

O'Neill H. S. C. (1991a) The origin of the Moon and the early history of the Earth-a chemical model. Part 1: The Moon. *Geochim. Cosmochim. Acta* **55**, 1135–1157.

O'Neill H. S. C. (1991b) The origin of the Moon and the early history of the Earth-a chemical model. Part 2: The Earth. *Geochim. Cosmochim. Acta* **55**, 1159–1172.

Parkinson I. J. and Pearce J. A. (1998) Peridotites from the Izu-Bonin-Mariana forearc (ODP Leg 125): Evidence for mantle melting and melt-mantle interaction in a supra-subduction zone setting. *J. Petrol.* **39**, 1577–1618.

Parkinson I. J. and Arculus R. J. (1999) The redox state of subduction zones: Insights from arc-peridotites. *Chem. Geol.* **160**, 409–423.

Pearson D. G., Carlson R. W., Shirey S. B., Boyd F. R., and Nixon P. H. (1995a) Stabilisation of Archaean lithospheric mantle: A Re-Os isotope study of peridotite xenoliths from the Kaapvaal craton. *Earth Planet. Sci. Lett.* **134**, 341–357.

Pearson D. G., Shirey S. B., Carlson R. W., Boyd F. R., Pokhilenko N. P., and Shimizu N. (1995b) Re-Os, Sm-Nd, and Rb-Sr isotope evidence for thick Archaean lithospheric mantle beneath the Siberian craton modified by multistage metasomatism. *Geoch. Cosmochim. Acta* **59**, 959–977.

Qu Q., Taylor L. A., and Xinmin Z. (1995) Petrology and geochemistry of mantle peridotite xenoliths from SE China. *J. Petrol.* **36**, 55–79.

Rapp R. P., Shimizu N., Norman M. D., and Applegate G. S. (1999) Reaction between slab-derived melts and peridotite in the mantle wedge: Experimental constraints at 3.8 GPa. *Chem. Geol.* **160**, 335–356.

Rollinson H. R. (1993) *Using Geochemical Data: Evaluation, Presentation, Interpretation.* Addison-Wesley Longman.

Rudnick R. L., McDonough W. F., and Orpin A. (1994) Northern Tanzanian peridotite xenoliths: A comparison with Kaapvaal peridotites and inferences of metasomatic reactions. In *Kimberlites, Related Rocks and Mantle Xenoliths*, Vol. 1A (eds. H. O. A. Meyer and O. H. Leonardos), pp. 336–353. CPRM Special Publication.

Smith D. and Boyd F. R. (1992) Compositional zonation in garnets in peridotite xenoliths. *Contrib. Mineral. Petrol.* **112**, 134–147.

Stolz A. J. and Davies G. R. (1988) Chemical and isotopic evidence from spinel lherzolite xenoliths for episodic metasomatism of the upper mantle beneath southeastern Australia. In *Oceanic and continental lithosphere: similarities and differences*, edited by M. A. Menzies, and K. G. Cox. *J. Petrol.* Special Lithosphere Issue. 303–330.

Suen C. J. and Frey F. A. (1987) Origins of the mafic and ultramafic rocks in the Ronda peridotite. *Earth. Planet. Sci. Lett.* **85**, 183–202.

Vaselli O., Downes H., Thirlwall M. F., Dobosi G., Coradossi N., Seghedi I., Szakacs A., and Vannucci R. (1995) Ultramafic xenoliths in Plio-Pleistocene alkali basalts from the eastern Transylvanian

Basin: Depleted mantle enriched by vein metasomatism. *J. Petrol.* **36**, 23–53.

Walter M. J. (1998) Melting of garnet peridotite and the origin of komatiite and depleted lithosphere. *J. Petrol.* **39**, 29–60.

Walter M. J. (1999) Melting residues of fertile peridotite and the origin of cratonic lithosphere. In *Mantle Petrology: Field Observations and High Pressure Experimentation: A Tribute to Francis R. (Joe) Boyd*, Vol. 6 (eds. Y. Fei, C. M. Bertka, and B. O. Mysen), pp. 225–239. Geochemical Society Special Publication.

Walker R. J., Carlson R. W., Shirey S. B., and Boyd F. R. (1989) Os, Sr, Nd, and Pb isotope systematics of southern African peridotite xenoliths: Implications for the chemical evolution of subcontinental mantle. *Geochim. Cosmochim. Acta* **53**, 1583–1595.

Winterburn P. A., Harte B., and Gurney J. J. (1989) Peridotite xenoliths from the Jagersfontein kimberlite pipe I, primary and primary-metasomatic mineralogy. *Geochim. Cosmochim. Acta* **54**, 329–341.

Wood B. J. and Virgo D. (1989) Upper mantle oxidation state: Ferric iron contents of lherzolite spinels by [57]Mössbauer spectroscopy and resultant oxygen fugacities. *Geochim. Cosmochim. Acta* **53**, 1277–1291.

Wood B. J., Bryndzia L. T., and Johnson K. E. (1990) Mantle oxidation state and its relationship to tectonic environment and fluid speciation. *Science* **248**, 337–345.

Wooden J. L. and Miller D. M. (1990) Chronologic and isotopic framework for early Proterozoic crustal evolution in the Eastern Mojave desert region, SE California. *J. Geophys. Res.* **95**, 20133–20146.

Yaxley G. M., Crawford A. J., and Green D. H. (1991) Evidence for carbonatite metasomatism in spinel peridotite xenoliths from western Victoria, Australia. *Earth Planet. Sci. Lett.* **107**, 305–317.

Zangana N. A., Downes H., Thirlwall M. F., Marriner G. F., and Bea F. (1999) Geochemical variation in peridotite xenoliths and their constituent clinopyroxenes from Ray Pic (French Massif Central): Implications for the composition of the shallow lithospheric mantle. *Chem. Geol.* **153**.

Table A1. Data used in study.[a]

	SiO$_2$	TiO$_2$	Al$_2$O$_3$	FeO*	MnO	MgO	CaO	Na$_2$O	K$_2$O	P$_2$O$_5$	Total*	V	
						Craton							
						Tanzania							
KAT1	45.54	0.11	0.65	7.04	0.11	45.97	0.39	0.07	0.09	0.04	100.0	18	XRF
LB1	44.52	0.08	0.40	6.48	0.12	48.09	0.25	0.00	0.04	0.02	100.0	14	XRF
LB11	43.97	0.04	0.86	7.33	0.13	47.33	0.31	0.00	0.04	0.00	100.0	25	XRF
LB12	44.47	0.05	2.02	8.50	0.15	42.90	1.82	0.02	0.05	0.02	100.0	44	XRF
LB14	42.14	0.08	0.33	7.30	0.12	49.91	0.04	0.00	0.08	0.01	100.0	13	XRF
LB16	43.87	0.14	0.61	7.38	0.13	47.36	0.41	0.00	0.07	0.03	100.0	21	XRF
LB17	45.16	0.25	0.57	7.56	0.14	45.79	0.43	0.00	0.07	0.02	100.0	28	XRF
LB18	42.36	0.11	0.43	8.46	0.13	48.04	0.39	0.00	0.06	0.01	100.0	18	XRF
LB19R	42.97	0.09	0.84	8.66	0.15	46.56	0.47	0.00	0.26	0.01	100.0	27	XRF
LB2	44.36	0.07	1.20	6.72	0.13	46.86	0.51	0.00	0.12	0.02	100.0	22	XRF
LB21	41.90	0.11	0.31	6.70	0.12	50.22	0.54	0.00	0.08	0.03	100.0	17	XRF
LB22	44.06	0.08	0.69	7.61	0.13	46.96	0.40	0.00	0.06	0.02	100.0	25	XRF
LB23	43.23	0.03	0.55	7.35	0.13	48.19	0.42	0.00	0.06	0.03	100.0	19	XRF
LB24	44.15	0.06	1.24	7.07	0.13	46.68	0.62	0.00	0.05	0.01	100.0	26	XRF
LB26	43.26	0.15	0.47	7.29	0.14	48.44	0.18	0.00	0.07	0.01	100.0	17	XRF
LB29	43.78	0.07	0.90	7.25	0.13	47.48	0.31	0.00	0.07	0.01	100.0	25	XRF
LB31	44.36	0.04	1.04	7.41	0.14	45.95	0.98	0.00	0.08	0.01	100.0	32	XRF
LB33	42.96	0.35	0.62	7.48	0.13	47.60	0.71	0.00	0.15	0.01	100.0	27	XRF
LB34	42.06	0.19	0.70	9.50	0.14	46.86	0.44	0.00	0.10	0.01	100.0	22	XRF
LB36	44.58	0.07	0.90	7.11	0.13	46.42	0.63	0.00	0.14	0.03	100.0	27	XRF
LB39	45.11	0.16	0.87	7.88	0.14	44.91	0.73	0.00	0.15	0.03	100.0	29	XRF
LB4	45.20	0.03	1.57	7.65	0.13	44.21	1.09	0.06	0.03	0.02	100.0	37	XRF
LB45	44.40	0.21	3.99	8.55	0.16	39.67	2.81	0.11	0.08	0.02	100.0	68	XRF
LB50-1	44.52	0.05	1.39	7.93	0.14	44.93	0.99	0.00	0.03	0.01	100.0	32	XRF
LB53	43.54	0.13	1.77	8.11	0.14	44.90	1.37	0.00	0.04	0.01	100.0	34	XRF
LB55	44.09	0.09	0.78	6.96	0.13	47.28	0.42	0.00	0.23	0.02	100.0	28	XRF
LB6	42.21	0.14	0.67	7.52	0.13	48.57	0.57	0.00	0.15	0.04	100.0	19	XRF
LB61	43.10	0.11	0.51	7.14	0.13	48.66	0.24	0.00	0.09	0.02	100.0	17	XRF
LB7	41.87	0.13	0.57	7.69	0.14	49.18	0.28	0.00	0.13	0.02	100.0	20	XRF
LB8	43.98	0.07	0.35	6.57	0.12	48.66	0.19	0.00	0.05	0.01	100.0	16	XRF
LB9	43.39	0.06	0.37	6.72	0.12	49.05	0.22	0.00	0.06	0.02	100.0	16	XRF
						Oceanic Mantle							
						Abyssal peridotites, Hole 920							
AP2	46.69	0.02	1.64	8.32	0.11	40.88	2.18	0.10	0.04	0.02	100.0	62	XRF
AP3	47.05	0.02	1.82	7.62	0.13	42.81	0.47	0.03	0.05	0.01	100.0	59	XRF
AP4	46.91	0.01	1.21	8.62	0.12	42.73	0.23	0.02	0.14	0.01	100.0	43	XRF
AP5	44.42	0.02	1.43	8.48	0.13	44.76	0.60	0.04	0.11	0.02	100.0	47	XRF
AP6	46.32	0.01	1.52	8.07	0.12	43.20	0.63	0.00	0.10	0.02	100.0	44	XRF
AP7	47.14	0.01	1.45	8.14	0.13	42.50	0.49	0.00	0.12	0.01	100.0	58	XRF
						Arc-related xenoliths							
						Simcoe, Cascades (Washington)							
2	44.35	0.00	1.30	7.66	0.13	45.52	1.02	0.02	0.01	0.01	100.0	23.4	ICP-MS
3	43.50	0.01	1.05	7.84	0.13	46.51	0.89	0.04	0.02	0.01	100.0	34.4	ICP-MS
5	46.81	0.06	1.76	7.68	0.13	42.52	0.88	0.14	0.01	0.02	100.0	34.9	ICP-MS
9c	44.19	0.02	1.45	7.67	0.13	45.32	1.10	0.09	0.02	0.02	100.0	27.2	ICP-MS
11	47.10	0.06	1.48	7.56	0.13	42.52	0.98	0.13	0.02	0.02	100.0	24.4	ICP-MS
12	44.03	0.04	1.27	7.70	0.12	45.90	0.90	0.01	0.01	0.01	100.0	26.4	ICP-MS
17	44.54	0.06	1.75	7.84	0.13	44.54	1.03	0.09	0.00	0.01	100.0	40.7	ICP-MS
20	43.72	0.02	0.48	8.56	0.13	46.80	0.21	0.07	0.00	0.01	100.0	7.3	ICP-MS
24	46.71	0.01	1.32	7.59	0.13	43.25	0.91	0.06			100.0	23.7	ICP-MS
25	46.69	0.00	1.19	7.25	0.13	43.76	0.93	0.05	0.00	0.01	100.0	16.8	ICP-MS
26	45.46	0.03	1.62	8.25	0.13	43.69	0.66	0.13	0.01	0.02	100.0	33.5	ICP-MS
28	46.73	0.01	1.31	7.70	0.13	43.21	0.82	0.08	0.00	0.01	100.0	27.6	ICP-MS
						Continental Peridotites							
						Southwestern USA							
Ba-4-42	45.11	0.14	4.36	7.96	0.13	38.28	3.60	0.39	0.01	0.01	100.0	77.9	ICP-MS
Ba 1-53	46.05	0.18	4.60	8.11	0.14	36.54	3.80	0.53	0.02	0.02	100.0	79.4	ICP-MS
Ba-5-8	44.51	0.04	2.53	8.14	0.13	42.43	2.08	0.12	0.01	0.01	100.0	46.5	ICP-MS
Ba-5-17	44.71	0.13	3.51	8.45	0.14	39.68	3.04	0.31	0.01	0.01	100.0	57.4	ICP-MS
DH-1	43.89	0.02	1.23	8.08	0.12	45.78	0.73	0.13	0.01	0.01	100.0	27.0	ICP-MS
DH-3	45.34	0.11	2.66	7.68	0.13	40.74	3.01	0.31	0.01	0.01	100.0	58.2	ICP-MS
DH-5	44.42	0.07	1.92	7.78	0.12	43.33	2.03	0.28	0.03	0.01	100.0	47.1	ICP-MS
DH-6	44.20	0.08	1.24	7.77	0.12	45.00	1.47	0.11	0.01	0.01	100.0	32.6	ICP-MS
DH-10	44.46	0.15	3.89	8.28	0.13	40.09	2.56	0.39	0.03	0.02	100.0	59.3	ICP-MS
DH-11	44.40	0.08	3.02	8.33	0.13	41.86	1.96	0.21	0.01	0.01	100.0	46.9	ICP-MS

(continued)

Table A1. (Continued)

	SiO$_2$	TiO$_2$	Al$_2$O$_3$	FeO*	MnO	MgO	CaO	Na$_2$O	K$_2$O	P$_2$O$_5$	Total*	V	
DH-13	44.07	0.13	2.93	8.45	0.14	41.18	2.82	0.24	0.02	0.01	100.0	61.2	ICP-MS
DH-14	43.01	0.11	2.49	9.16	0.14	42.44	2.39	0.23	0.02	0.01	100.0	46.4	ICP-MS
DH-20	44.39	0.05	2.29	8.08	0.13	43.07	1.77	0.20	0.01	0.01	100.0	45.0	ICP-MS
DH-37	44.97	0.05	2.60	8.02	0.13	41.98	2.01	0.22	0.01	0.01	100.0	49.4	ICP-MS
KiL-1	44.47	0.11	3.20	8.32	0.13	40.83	2.59	0.32	0.01	0.02	100.0	54.7	ICP-MS
KiL-2	44.94	0.11	3.37	8.27	0.13	40.13	2.75	0.27	0.01	0.01	100.0	54.4	ICP-MS
Kil-3	45.48	0.14	3.75	8.27	0.14	38.57	3.25	0.37	0.01	0.01	100.0	71.2	ICP-MS
Kil-4	45.36	0.12	3.73	8.34	0.13	39.15	2.75	0.39	0.01	0.01	100.0	63.7	ICP-MS
Kil-8	45.23	0.15	3.59	8.40	0.14	39.39	2.81	0.27	0.00	0.01	100.0	64.6	ICP-MS
KiL-41	44.00	0.08	2.13	9.08	0.14	43.10	1.30	0.14	0.01	0.01	100.0	38.4	ICP-MS
Kil-43	45.15	0.10	3.34	8.12	0.13	40.25	2.62	0.26	0.01	0.01	100.00	57.2	ICP-MS
Kil-44	45.64	0.13	3.81	8.19	0.14	38.49	3.24	0.33	0.01	0.01	100.00	67.7	ICP-MS
KiL-70	44.82	0.12	3.75	8.26	0.13	39.35	3.13	0.42	0.00	0.01	100.0	62.5	ICP-MS
KiL-71	45.21	0.11	3.22	7.99	0.13	40.37	2.60	0.34	0.01	0.01	100.0	54.0	ICP-MS
LC-1	42.72	0.05	0.92	9.15	0.14	46.05	0.75	0.18	0.02	0.01	100.0	22.5	ICP-MS
LC-25	44.50	0.05	1.31	7.95	0.13	44.61	1.27	0.14	0.02	0.02	100.0	35.7	ICP-MS
LC-47	44.55	0.12	3.53	8.09	0.13	40.79	2.48	0.28	0.01	0.02	100.0	57.8	ICP-MS
LC-52	42.56	0.03	0.79	8.53	0.12	47.21	0.68	0.06	0.01	0.01	100.0	22.7	ICP-MS
LC-62	41.04	0.10	1.03	11.33	0.16	44.19	1.88	0.22	0.02	0.02	100.0	33.0	ICP-MS
LC-69	43.25	0.11	1.78	8.53	0.13	44.34	1.44	0.33	0.06	0.03	100.0	37.5	ICP-MS
VT-6	43.49	0.03	1.15	8.15	0.13	46.29	0.59	0.15	0.01	0.01	100.0	17.9	ICP-MS
VT-18	46.21	0.03	2.19	7.89	0.13	41.77	1.63	0.13	0.01	0.01	100.0	39.2	ICP-MS
VT-26	43.15	0.01	1.06	7.32	0.11	48.11	0.20	0.03	0.00	0.01	100.0	12.8	ICP-MS
VT-29	45.54	0.02	1.41	7.03	0.11	44.92	0.78	0.18	0.01	0.01	100.0	27.6	ICP-MS
VT-30	42.97	0.03	0.67	7.71	0.12	47.24	1.19	0.06	0.01	0.01	100.0	13.7	ICP-MS

[a] FeO* = total FeO and Fe$_2$O$_3$; total* = all data normalized to 100%; oxides in wt %; (Ba, DH from Dish Hill in California, KIL from Kilbourne Hole in New Mexico, LC from Lunar Crater in Nevada, and VT from Vulcan's Throne in Arizona).